

# STUDYING THE IMPACT OF XENON GAS IN URANIUM-MOLYBDENUM FUEL

---

A Dissertation Proposal

presented to

the Faculty of the Graduate School

at the University of Missouri

---

In Partial Fulfillment

of the Requirements for the Degree

Doctor of Philosophy

---

by

ABU RAFI MOHAMMAD IASIR

Dr. Karl Hammond, Dissertation Supervisor

APRIL, 12 2019

# TABLE OF CONTENTS

<b>LIST OF TABLES.....</b>	<b>iv</b>
<b>LIST OF FIGURES .....</b>	<b>v</b>
<b>Chapter</b>	
<b>1. U–MO FUEL: A BRIEF INTRODUCTION .....</b>	<b>1</b>
<b>2. EFFECT OF XENON ON THE OVERALL THERMAL CONDUCTIVITY OF U-10MO .....</b>	<b>6</b>
2.1 Introduction .....	6
2.2 Methods .....	8
2.2.1 Effective Thermal Conductivity Calculation .....	11
2.3 Results and Discussion .....	13
2.3.1 Effect of Xenon Gas Bubbles on the Thermal Conductivity .....	13
2.3.2 Effect of Xenon Pressure on the Overall Thermal Conductivity .....	16
2.3.3 Effect of Bubble Arrangement on Thermal Conductivity .....	17
2.4 Conclusions .....	21
<b>3. FIRST-PRINCIPLES STUDY OF METALLIC URANIUM .....</b>	<b>26</b>
3.1 Introduction .....	26
3.2 Density Functional Theory: A Brief Introduction .....	28
3.2.1 Solution of the Single particle Kohn-Sham Equations .....	31
3.3 Kohn-Sham problem for an isolated atom .....	32
3.4 Theory of Pseudopotential .....	34
3.4.1 Basic Phillips-Kleinman Construction .....	36
3.5 Computational Details .....	39
3.6 Results .....	40

3.6.1	$\alpha$ -Uranium .....	41
3.6.2	$\gamma$ -U: Crystal Structure and Elastic Moduli .....	43
3.6.3	Body-centered Tetragonal Uranium .....	45
3.6.4	Face-Centered Cubic Uranium .....	46
3.6.5	Electronic Density of States .....	47
3.7	Conclusion .....	49
<b>4.</b>	<b>XENON MOBILITY IN U-MO FUEL .....</b>	<b>55</b>
<b>Appendix</b>		
<b>A.</b>	<b>CALCULATION OF ELASTIC PARAMETERS OF ALPHA-URANIUM .....</b>	<b>58</b>

## LIST OF TABLES

Table	Page
3.1 Parameters used to generate the pseudopotential in atompaw .....	40
3.2 Comparison of ground-state properties and elastic moduli of $\alpha$ -U with previous work .....	43
3.3 Comparison of ground-state properties and elastic moduli of $\gamma$ -U with previous work .....	44
3.4 Comparison of ground-state properties and elastic moduli of bct uranium with previous work .....	45
3.5 Comparison of ground-state properties and elastic parameters of fcc uranium .....	46

## LIST OF FIGURES

Figure	Page
1.1 Schematic of monolithic and dispersion fuel .....	3
2.1 Discretized domain of intra-granular xenon bubbles .....	9
2.2 SEM image of the fission gas bubbles along the grain boundary .....	11
2.3 Thermal conductivity of xenon as a function of pressure and temperature .....	12
2.4 Comparision between the thermal conductivities.....	13
2.5 Comparison of thermal conductivities with theoretical models .....	15
2.6 Comparing thermal conductivities between the inclusion of GB xenon and withouth xenon .....	16
2.7 Overall thermal conductivity of U-10Mo using the thermal conductivity of xenon at two extremes of pressure (1 bar and 1000 bar) .....	17
2.8 Different bubble arrangements in which the area of each bubble and the number of bubbles are the same .....	18
2.9 Comparison of the calculated thermal conductivity of different bubble ar- rangements (constant bubble area and diameter) .....	19
2.10 Different bubble arrangements where the area is the same but the bubbles have different diameters.....	20
2.11 Comparison of thermal conductivity between different bubble diameters at constant total bubble area with bubble-free U-10Mo. ....	20
3.1 Schematic representation of the self-consistent loop solution of Kohn-Sham equations. ....	33
3.2 Radial distribution function of Hydrogenic 1s, 2s and 3s electron. It shows higher kinetic energy near the nucleus. ....	35

3.3	Schematic diagram of the replacement of all-electron wave function and core potential by a pseudo-wavefunction and pseudopotential. ....	35
3.4	Energy vs volume plot for $\alpha$ -uranium .....	42
3.5	Total electronic densities of states of $\alpha$ , $\gamma$ , bct, and fcc uranium near the Fermi level. ....	47
3.6	The partial electronic densities of states of $\alpha$ , $\gamma$ , bct, and fcc uranium near the Fermi level. ....	48

## CHAPTER 1

### U–MO FUEL: A BRIEF INTRODUCTION

The Reduced Enrichment for Research and Test Reactors (RERTR) [1] program was initiated in the USA in the late 1970s to develop new nuclear fission fuels to replace high-enriched uranium (HEU). The RERTR is now managed by the U.S. National Nuclear Security Administration (NNSA) office of Material Management and Minimization (M<sup>3</sup>). The development of low-enrichment uranium (LEU) fuels for high-performance reactors is an important nonproliferation initiative as it explained in [2] “*Material Management and Minimization program reduces the risk of highly enriched uranium and plutonium falling into the hands on nonstate actors by minimizing the use of and, when possible, eliminating weapons-usable nuclear material around the world*”. This initiative has completed a total of 69 reactors conversions to the use of LEU fuel. In addition, 26 reactor facilities have been verified to have been shut down [3]. The conversion of six domestic high performance research reactors <sup>1</sup> that still use Highly Enriched Uranium fuel is yet to be achieved. Due to their unique operating conditions, converting these six reactors is not easy and created a plethora of nuclear engineering challenges. These conversion process may take longer time periods, but developing a new LEU fuel is essential to ensure better performance.

Research reactors operate at relatively low peak fuel temperatures, but are required to meet fuel performance requirements at high burnup. A typical peak fuel centerline temperature is around 250°C. For a research reactor fission densities are usually in the range of

---

<sup>1</sup> Advance Test Reactor at INT, Idaho; Advanced Test Reactor Assembly at INL, Idaho; High Flux Isotope Reactor at ORNL, Tennessee; Massachusetts Institute of Technology Reactor, Massachusetts; National Bureau of Standards Reactor in Gaithersburg, Maryland; University of Missouri Research Reactor in Columbia, Missouri.

$3 \times 10^{21}$  to  $6 \times 10^{21}$  f/cm<sup>3</sup>. In some cases, peak fuel fission density exceeds  $7 \times 10^{21}$  f/cm<sup>3</sup>, requiring a higher number of initial <sup>235</sup>U atoms. There are a few number of uranium alloys that have the combination of high uranium density and stable fuel behavior to the high burnup to replace the high power density reactors. As it appears, one of the main requirements of LEU fuels is increased uranium density, such as that found in metallic uranium, to offset the decrease in <sup>235</sup>U enrichment. Metallic uranium is thought to have sufficient density, but the orthorhombic crystal structure of  $\alpha$ -U and the anisotropic fuel swelling that results make it unattractive as a fuel. Uranium alloys that retain the high-temperature  $\gamma$ -phase, which is body-centered cubic, are more suitable for reactor fuel due to their more isotropic radiation-induced swelling behavior compared with  $\alpha$ -uranium [4].

Various uranium alloys have been tested as alternative metallic fuels under reactor operating conditions, including U<sub>6</sub>Fe and U<sub>6</sub>Mn [5, 6]. Elements such as molybdenum (Mo), niobium (Nb), titanium (Ti), and zirconium (Zr) have also been tried as alloying elements because of their solubility in  $\gamma$ -uranium [7, 8, 9]. Molybdenum stabilizes uranium's  $\gamma$ -phase at concentrations near the eutectoid point, lowering the phase transition temperature from 776 °C for pure uranium (corresponding to the  $\beta$ - $\gamma$  allotropic point) to the eutectoid point of 555 °C for 11.1 percent molybdenum in  $\gamma$ -uranium [10, 11]. To take advantage of this, uranium alloyed with 10 wt% molybdenum (U-10Mo) is currently being developed as a potential high-density LEU fuel for high-performance research reactors.

Before the current interest in U-Mo metallic fuel, some of the earlier nuclear reactors used metallic fuel because of the combination of high uranium density and metallic properties. The Godiva IV pulsed reactors at Los Alamos (initially known as *Lady Godiva*) used U-Mo alloys, which dates back to 1960. The Fast Burst Reactor (FBR) at White Sands, the Army Pulsed Radiation Facility (Aberdeen, MD), and the Sandia Pulsed Reactor II used U-Mo alloys. All of these reactors utilized the  $\gamma$  phase of uranium, but because of the short irradiation time the impacts of fuel burnup were minimal [12]. The Dounreay Fast Reactor used a number of metal-fuel-based designs, which included U-9.1 wt% Mo



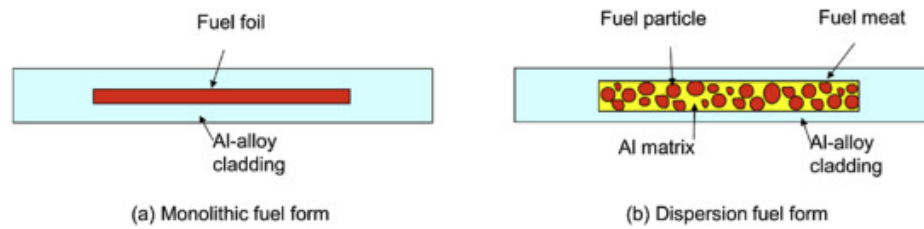


**Figure 1.1.** Schematic diagram for monolithic and dispersion fuel from Jeong *et al.* [15]

and U-7 wt% Mo clad in niobium. The highly alloyed fuel cracked more, even though the 9.1-wt%-Mo fuel swelled slightly less than 7 wt%-Mo alloy [13]. In U.S. the Enrico Fermi Fast Breeder Reactor (EFFBR) was the first commercial fast reactor that used U-10Mo fuel. The primary concern was to ensure that the fuel would maintain  $\gamma$ -phase stability during the operating condition. A series of experiments have been performed and mapped the fission rate and temperature dependence of  $\gamma$ -phase stability [14]. Two types of U-Mo alloy fuel have been designed and tested. One is monolithic fuel form, in which a thin layer of U-Mo foil is bonded to aluminum clad. The other is a dispersion fuel form, where U-Mo/Al, composed of U-Mo fuel particles that are dispersed in an inert Al matrix.

For five decades, the dispersion fuel has powered many test and research reactors worldwide. The manufacturing process and operating conditions are well known for these types of fuels. One of the first experimental work performed for U-Mo fuel was performed on U-Mo dispersion fuel. The high-burnup testing of the dispersion fuel showed a pattern of breakaway swelling (also called ‘blistering’ or ‘pillowing’) behavior at intermediate burnup. The post-irradiation examination (pie) of the U-Mo dispersion fuel revealed that this phenomenon is due to fission gas released from the interaction layer. Reaction between the U-Mo and aluminum occurs during irradiation and forms a ternary aluminide  $[(U-Mo)Al_x]$  phase which releases the fission gas at the boundary between the interaction phase and the aluminum matrix [16, 17, 18, 19]. These gas bubbles have tendency to aggregate into the gas pockets, which weakens the fuel meat by exerting internal gas pressure. The result is a mechanical failure and large increase of the fuel volume. To eliminate the fuel matrix

interaction the ‘monolithic’ U–Mo fuel was suggested. In monolithic fuels, a zirconium foil is used as a diffusion barrier between the fuel and the cladding (aluminum) to prevent diffusion of molybdenum into the cladding [17].

In the current work we have investigated how fission gas (xenon and krypton) impacts the U–Mo fuel. In the second chapter we have studied the reduction of thermal conductivity due to the presence of xenon gas. We have implemented finite element method to study the different microstructural configuration of fission gas in U–Mo fuel. In the third chapter we have introduced a new *pseudopotential* for metallic uranium to study the properties using first-principles (Density Functional Theory (DFT)) method. In the fourth chapter we will discuss about the atomistic diffusion mechanism of xenon in U–Mo fuel, which includes the study of xenon gas in the U–Mo fuel using DFT methods.

## References

1. James L. Snelgrove, G. L. Hofman, M. K. Meyer, C. L. Trybus, and T. C. Wiencek. Development of very-high-density low-enriched-uranium fuels. *Nucl. Eng. Des.*, 178(1):119–126, 1997.
2. National Nuclear Security Administration. Material management minimization. <https://www.energy.gov/nnsa/missions/nonproliferation>, 2019.
3. EH Wilson, A Bergeron, JA Stillman, TA Heltemes, D Jaluvka, and L Jamison. Us high performance research reactor conversion program: an overview on element design. In *Proceedings of the 2017 European Research Reactor Conference*. RRFM Rotterdam, Netherlands, 2017.
4. J. H. Kittel, B. R. T. Frost, J. P. Mustelier, K. Q. Bagley, G. C. Crittenden, and J. Van Dievoet. History of fast reactor fuel development. *J. Nucl. Mater.*, 204:1–13, 1993.
5. M. K. Meyer, T. C. Wiencek, S. L. Hayes, and G. L. Hofman. Irradiation behavior of U<sub>6</sub>Mn–Al dispersion fuel elements. *J. Nucl. Mater.*, 278(2):358–363, 2000.
6. G. L. Hofman, R. F. Domagala, and G. L. Copeland. Irradiation behavior of low-enriched U<sub>6</sub>Fe–Al dispersion fuel elements. *J. Nucl. Mater.*, 150(2):238–243, 1987.
7. G Donzé and G Cabane. Stabilisation de la phase  $\gamma$  dans les alliages ternaires a base d’uranium-molybdene. *J. Nucl. Mater.*, 1(4):364–373, 1959.

8. F Giraud-Heraud and J Guillaumin. Transition phase formation in U-7,5% Nb-2,5%Zr alloy. *Acta Metall.*, 21(9):1243–1252, 1973.
9. Denise Adorno Lopes, Thomaz Augusto Guisard Restivo, and Angelo Fernando Padilha. Mechanical and thermal behaviour of U–Mo and U–Nb–Zr alloys. *J. Nucl. Mater.*, 440(1):304–309, 2013.
10. Hiroaki Okamoto, Mark E. Schlesinger, and Erik M. Mueller, editors. *Mo (Molybdenum) Binary Alloy Phase Diagrams*, volume 3 of *ASM Handbook*, pages 489–498. ASM International, 2016.
11. A. Berche, N. Dupin, C. Guéneau, C. Rado, B. Sundman, and J. C. Dumas. Calphad thermodynamic description of some binary systems involving U. *J. Nucl. Mater.*, 411:131–143, 2011.
12. J. A. Horak, J. A. Reuscher, and D. J. Sasmor. Operating experience with uranium–molybdenum fuel in pulsed reactors. Technical report, Sandia Labs., Albuquerque, N. Mex.(USA), 1973.
13. S. A. Cottrell, E. Edmonds, P. Higginson, and W. Oldfield. Development and performance of dounreay fast reactor metal fuel. Technical report, United Kingdom Atomic Energy Authority. Industrial Group. Dounreay, 1964.
14. International Atomic Energy Agency. Development status of metallic, dispersion and non-oxide advanced and alternative fuels for power and research reactors. *Nuclear Fuel Cycle and Material Section*, 2003.
15. Gwan Yoon Jeong, Yeon Soo Kim, and Dong-Seong Sohn. Mechanical analysis of UMo/Al dispersion fuel. *J. Nucl. Mater.*, 466:509–521, 2015.
16. Ann Leenaers, S. Van den Berghe, E. Koonen, C. Jarousse, F. Huet, M. Trotabas, M. Boyard, S. Guillot, L. Sannen, and M. Verwerft. Post-irradiation examination of uranium–7wt% molybdenum atomized dispersion fuel. *J. Nucl. Mater.*, 335(1):39–47, 2004.
17. Jan-Fong Jue, Dennis D. Keiser, Cynthia R. Breckenridge, Glenn A. Moore, and Mitchell K. Meyer. Microstructural characteristics of hip-bonded monolithic nuclear fuels with a diffusion barrier. *J. Nucl. Mater.*, 448(1):250–258, 2014.
18. Sven Van den Berghe, Wouter Van Renterghem, and Ann Leenaers. Transmission electron microscopy investigation of irradiated U–7wt% Mo dispersion fuel. *J. Nucl. Mater.*, 375(3):340–346, 2008.
19. D. Olander. Growth of the interaction layer around fuel particles in dispersion fuel. *J. Nucl. Mater.*, 383(3):201–208, 2009.

## **CHAPTER 2**

### **EFFECT OF XENON ON THE OVERALL THERMAL CONDUCTIVITY OF U-10MO**

#### **2.1 Introduction**

Thermal conductivity is an important property of any nuclear fuel, since most of the important physical properties are temperature-dependent. In the case of high-performance reactors, fuels must undergo high fission density at relatively low temperatures. For this reason, research reactor fuels are designed for efficient heat rejection. During test operations, Burkes and coworkers [1] observed that the thermal conductivity in monolithic fuels decrease significantly with increased burnup. For a fission density of  $3.30 \times 10^{21} \text{ cm}^{-3}$  at 200 °C, thermal conductivity decreased by approximately 30%; at  $4.53 \times 10^{21} \text{ cm}^{-3}$ , conductivity decreased by 45% [1].

Fission also creates a variety of fission products, which result in gas bubbles, metallic precipitates, and solutes in the fuel matrix [2]. These fission products, in addition to radiation damage in reactor environments, result in complex microstructural evolution that restructures the nuclear fuel over time. Fission gas bubbles are particularly problematic, as they cause changes in thermal conductivity and swelling of the fuel. In addition,  $^{135}\text{Xe}$  is a potent neutron absorber.

For every four fission events, an average of one inert gas atom (xenon or krypton) is produced. The dominant gaseous species is xenon, accounting for almost 85% of fission gas [3, 4]. Xenon atoms in U–Mo alloy fuels have a strong tendency to precipitate into small bubbles due to their low solubility. The formation and growth of gas bubbles inside irradi-

ated nuclear fuels has technical importance, as bubbles influence the microstructure of the material [5]. Recent TEM and SEM images show that fission bubbles in U-10Mo distribute themselves in both inter-granular and intra-granular formations [6, 7, 8, 9]. High-fission-density fuels show randomly-distributed, micrometer-sized fission gas bubbles distributed throughout the grains [9]. Inter-granular bubble density increases with burnup.

Inside the micrometer-sized grains, fission gas forms superlattices [9, 6, 7], similar to those seen in ion-irradiated materials [10, 11, 12, 13, 14, 15, 16, 17, 18, 19]. Typical bubble sizes are 2–6 nm in diameter, and the distance between the bubbles is typically in the 4–12 nm range. The superlattice usually has the same crystal structure as the host material, but an exception exists: the superlattice in U-10Mo shows a face-centered cubic structure in a body-centered cubic matrix. An ion-irradiated bubble superlattice has a lattice parameter of tens of nanometers [6]; that of fission gas bubbles is typically similar [20].

The thermal conductivity of a monolithic U–Mo fuel plate is at a maximum prior to irradiation [1]. Inclusions and porosity change the thermal and the electrical conductivity of many materials [21]. Solid fission products usually have minimal impact on overall thermal conductivity, as their conductivities are similar to the conductivity of the fuel. Gases, on the other hand, have much lower thermal conductivity than the matrix, and typically have much lower densities and heat capacities as well. Various models, both empirical and theoretical, have been proposed to describe the changes in conductivity due to gas bubbles. Maxwell [22] was among the first to derive an expression for the effective thermal conductivity of heterogenic media; his model assumed uniform distribution of spherical particles in a matrix. A few other empirical models also exist [23, 24, 25]; unfortunately, the large diversity of pore shape, pore size, and type of included material inside nuclear fuel make it impossible to describe heat transfer with a single equation. Several theoretical models have been proposed to describe the influence of porosity and inclusions on the thermal conductivity [22, 26, 27, 28, 29]. These theoretical models usually assume pores

with regular geometric shapes, and that the pore arrangement is sufficiently dilute so as to neglect interaction between inclusions.

The microstructure of irradiated nuclear fuels is very complicated due to the lack of consistency between bubbles. The intra-granular gas bubbles are two or three order of magnitude smaller than the inter-granular gas bubbles [30]. The shapes of the bubbles are also highly variable: the intra-granular gas bubbles are approximately spherical, whereas inter-granular gas bubbles do not have consistent shapes. In this work, we assess contributions to the thermal conductivity of U-10Mo from both inter- and intra-granular gas bubbles. The impact of xenon bubble pressure on the overall thermal conductivity is also estimated. At the end, we present a study of the influence of different bubble arrangements on the overall thermal conductivity.

## 2.2 Methods

A finite element model was used to solve the steady-state heat conduction equation in the presence of various microstructures. Two types of microstructures containing xenon gas bubbles were used: a xenon bubble superlattice structure representing intra-granular bubbles, and a grain boundary structure representing inter-granular bubbles. Figure 2.1 shows an example of an intra-granular bubble distribution, while Figure 2.2 shows the inter-granular bubble distribution. In the intra-granular bubble case, xenon gas bubbles were placed in a variety of spatial configurations, including configurations consistent with a gas bubble superlattice. All simulations were performed in a two-dimensional domain. The gas bubble superlattice structure was created based on data from Miller et al. [6]. According to Miller et al. [6], the bubble size inside the grain boundary superlattice structure is normally distributed. Based on their experimental values, we chose four bubble diameters to create our simulation. Since the superlattice in U-10Mo is FCC, the two-dimensional structure of bubbles was created based on the FCC structure with a 12 nm lattice parameter, which was also taken from Miller et al. [6]. The bubble sizes were randomly sampled from

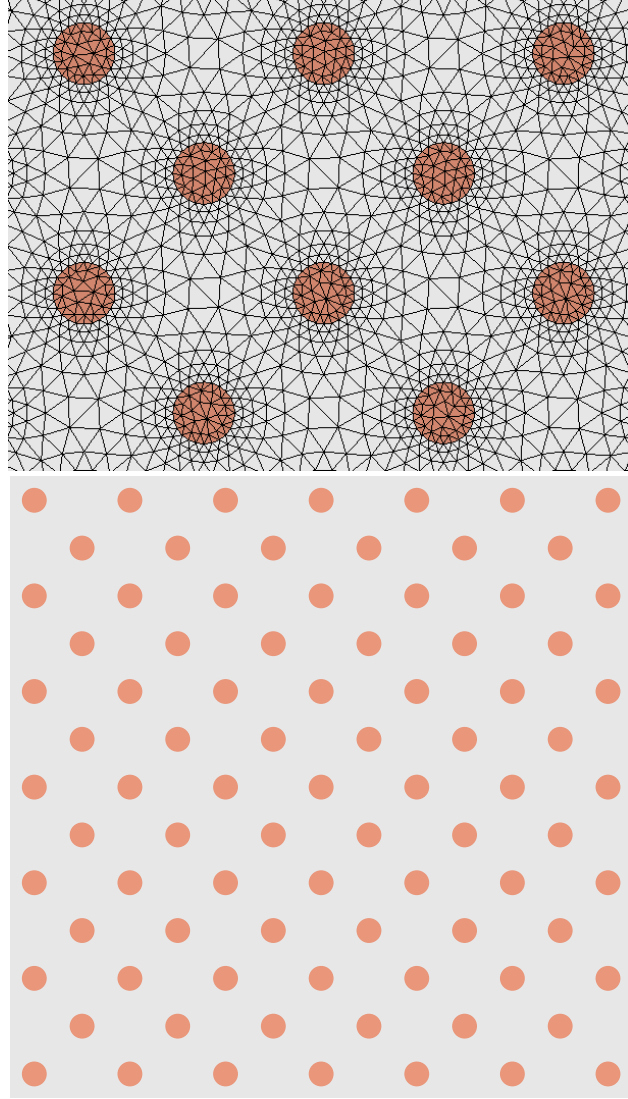


**Figure 2.1.** (a) Discretized domain of intra-granular xenon bubbles inside a U-10Mo matrix; (b) Example two-dimensional bubble distribution used for intra-granular xenon gas, consisting of bubbles with 3.1, 3.6, 3.75, and 4.0 nm diameters, consistent with the work of Miller and coworkers [6]. The lattice parameter for the gas bubble superlattice is 12.0 nm.

this distribution using the discrete values of 3.1, 3.6, 3.75, and 4.0 nm in diameter. The square domain's dimensions were 80 nm  $\times$  80 nm, which results in 85 bubbles with a lattice constant of 12 nm. Triangular elements were used to create the mesh using the Trelis Pro software package [31].

In the inter-granular bubble case, the grain boundary structure of U-10Mo was created based on images from Miller et al. [7]. Their SEM (Scanning Electron Micrograph) of a Focused Ion Beam (FIB) cross-section showed fission gas bubbles populating the grain boundaries, as shown in Figure 2.2. This domain was also discretized with triangular elements. The top and bottom boundaries of the domain of the FEM domain were assumed to be adiabatic. The left and right boundary have fixed-temperature boundary conditions applied. This temperature difference drives the heat flow.

The thermal conductivity of U-10Mo was estimated from a linear fit of thermal conductivity as a function of temperature between 298 K and 1073 K from Kaufmann [33]. Burkes et al. [34] also provided a linear fit of the U-10Mo thermal conductivity as a function of temperature up to 873 K; their results were in good agreement with Kaufmann's [33]. The thermal conductivity of xenon depends on both temperature and pressure [32], as shown in Figure 2.3. The pressure inside a bubble depends on the radius of the bubble, the surface tension, the magnitude of the Burgers vector, and the shear modulus of the host material [35, 36]. According to Xiao et al. [37], the pressure inside a xenon bubble can be as high as 120 kbar. Such high pressures suggest the possibility of forming solid xenon bubbles inside the fuel [38, 39, 40]. Unfortunately, thermal conductivity data for xenon above 1000 bar are not available, so we chose two limiting sets of thermal conductivity data: 1 bar and 1000 bar. For each set of data, a polynomial fit (fifth order) was used to interpolate the conductivity over the temperature range.



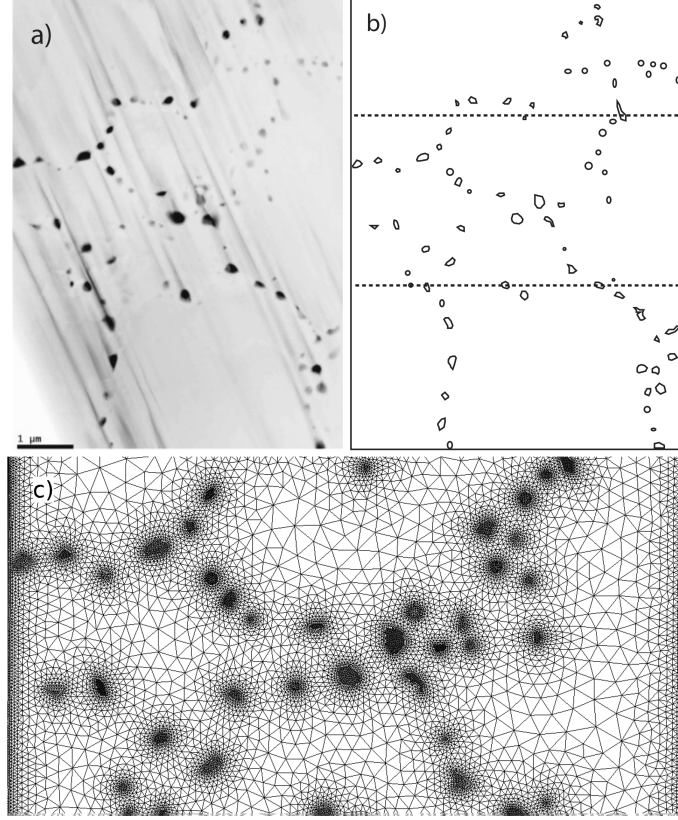


**Figure 2.2.** (a) SEM image of the fission gas bubbles along the grain boundaries from Miller et al. [7] used for FEM calculations [7] (b) Geometry created based on the grain boundary fission gas image in (a) (c) FEM mesh with grain boundary fission gas of the region between the dotted line in (b)

### 2.2.1 Effective Thermal Conductivity Calculation

The temperature in a composite material in the absence of heat source is described by the heat equation:

$$\nabla \cdot (K \nabla T) = 0 \quad (2.1)$$

where  $K(x, y) = \chi_1(x, y)K_1 + \chi_2(x, y)K_2$  is the thermal conductivity tensor,  $T$  is the temperature,  $K_i$  ( $i = 1$  for the matrix and 2 for the bubble) is the thermal conductivity tensor, and  $\chi_i(x, y)$  is the indicator function of phase  $i$ . Local heat flux can be calculated using the equation

$$q''(x, y) = -K(x, y) \cdot \nabla T(x, y) \quad (2.2)$$

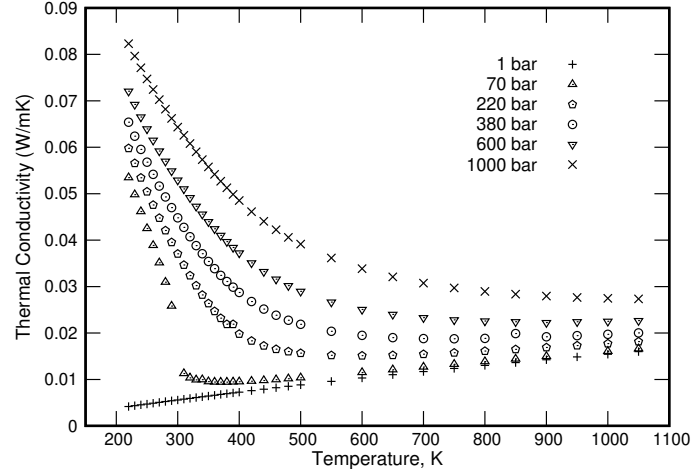


**Figure 2.3.** Thermal conductivity of xenon as a function of pressure and temperature based on the measurements of Rabinovich et al. [32]. Note that the critical point of xenon is 289.733 K and 58.42 bar; this is why there is such a drastic change in conductivity at low temperature between the 1 bar and 70 bar isobars.

where  $q''(x, y)$  is the local heat flux vector and  $\nabla T(x, y)$  is the local temperature gradient. Local temperature and heat flux are calculated by solving Equation (2.1) and (2.2). The components of the effective thermal conductivity tensors are calculated via

$$K_{\text{eff}}^x = -q''_x \left\langle \frac{\partial x}{\partial T} \right\rangle \quad (2.3)$$

Where  $q''_x$  is the mean heat flux in the  $x$  direction, and  $\left\langle \frac{\partial x}{\partial T} \right\rangle$  is the average inverse temperature gradient in the  $x$  direction. The MOOSE Framework [41] was used to solve Equation (2.1) with Dirichlet boundary conditions at  $x = 0$  and  $x = L$  and Neumann (adiabatic) boundary conditions at  $y = 0$  and  $y = L$ . The effective thermal conductivity was calculated using Equation (2.3).

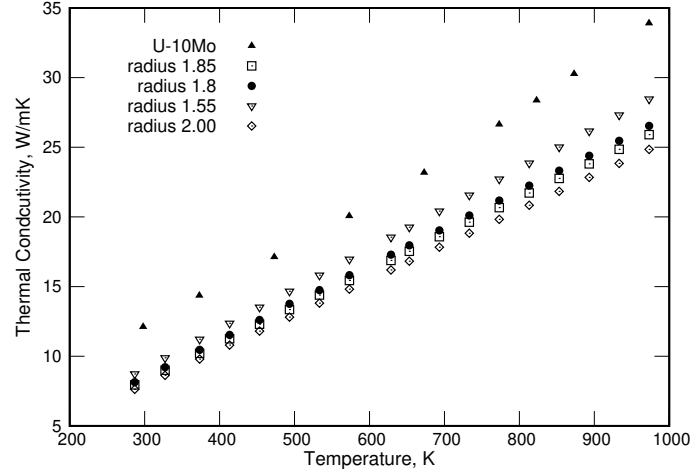


**Figure 2.4.** Comparison between the thermal conductivity of U-10Mo (from Kaufmann [33]) to the effective thermal conductivity of U-10Mo with intra-granular xenon bubbles of different diameters as arranged in Figure 2.1b.

## 2.3 Results and Discussion

### 2.3.1 Effect of Xenon Gas Bubbles on the Thermal Conductivity

We examined two broad categories of bubbles: inter-granular bubbles (i.e., bubbles that collect at grain boundaries), and intra-granular bubbles. The intra-granular case is intended to represent the effect of a gas bubble superlattice (GBS) on the conductivity. We will discuss each case in turn.

#### 2.3.1.1 Intra-Granular Bubbles

A two-dimensional representation of a gas bubble superlattice, as shown in Figure 2.1, was used to simulate the effect of intra-granular bubbles on the thermal conductivity. Five different bubble sizes were used, each with the same superlattice constant (resulting in the same center-center distance between bubbles). Figure 2.4 shows the effective thermal conductivity due to the xenon bubble distribution in the intra-granular region. As is clear from Figure 2.4, the thermal conductivity decreases with increasing bubble size, and is 20–40 percent lower in all cases than it is for bubble-free U-10Mo. In these simulations, the thermal conductivity of xenon was assumed constant at its 1 bar value (it is still a

function of temperature). Figure 2.5 shows the result of the finite element method solution compared with the theoretical solution for porous materials' thermal conductivity from the Maxwell–Eucken equation [22],

$$\lambda = \lambda_s \frac{\lambda_p + 2\lambda_s + 2\nu_p(\lambda_p - \lambda_s)}{\lambda_p + 2\lambda_s - \nu_p(\lambda_p - \lambda_s)}, \quad (2.4)$$

where  $\lambda$  is the effective thermal conductivity of the fuel,  $\lambda_s$  is the thermal conductivity of the continuous phase (U-10Mo),  $\lambda_p$  is the thermal conductivity of the dispersed phase (xenon bubble),  $\nu_p$  is the volume fraction of the dispersed phase (i.e., the volume fraction of xenon in U-10Mo). Equation (2.4) assumes the pore volume fraction is less than 15 percent, that the pores are dispersed uniformly in the solid, and that the distance between the pores is large enough that they do not interact [42, 43]. The result is also compared with the Hashin–Shtrikman upper bound, which is based on a theoretical expression derived for the magnetic permeability of a multiphase material [44],

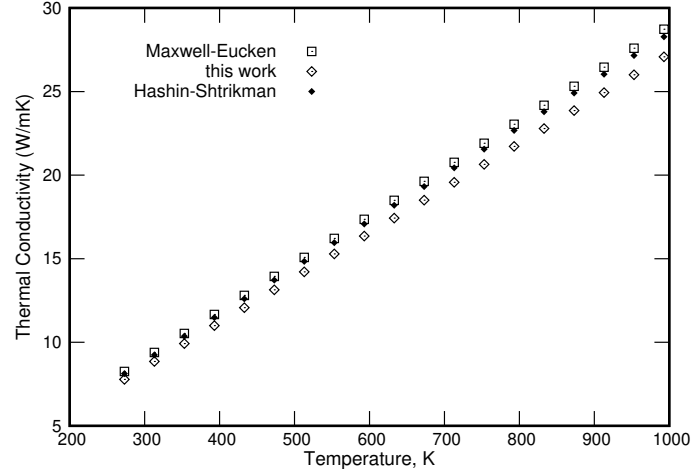
$$\lambda = \frac{1}{4} \left[ \lambda_p(3\nu_p - 1) + \lambda_s(2 - 3\nu_p) + \left( \left[ \lambda_p(3\nu_p - 1) + \lambda_s(2 - 3\nu_p) \right]^2 + 8\lambda_s\lambda_p \right)^{\frac{1}{2}} \right]. \quad (2.5)$$

Figure 2.5 shows the effect of distributed gas bubbles in the intra-granular region (grain boundary bubbles were not included). Both theoretical models over-predict the conductivity by 5–10 percent, and the absolute error increases with temperature.

### 2.3.1.2 Inter-Granular Bubbles

Inter-granular fission gas bubbles are associated with bubbles that collect on or near grain boundaries. Bubbles are naturally drawn to grain boundaries because of the excess volume that accompanies grain boundaries, as well as the decreased energy associated with void formation at grain boundaries relative to the bulk.

To evaluate the effect of inter-granular fission gas on the overall thermal conductivity, Figure 2.2b was used as the simulation domain. As can be seen in Figure 2.2, fission gas



**Figure 2.5.** Comparison of the calculated effective thermal conductivity of U-10Mo with intra-granular xenon bubble (radius 1.55 nm, 10% porosity) with the Maxwell–Eucken [22] and Hashin–Shtrikman [44] models. In all cases, we find that the two theoretical models over-predict the thermal conductivity by about 5–10 percent compared with the numerical solution.

bubbles trapped on grain boundaries do not have consistent shapes. Note that this is only a snapshot in time of the grain structure: as burnup increases, the stress in the fuel changes, more fission gas is evolved, and the grains can rotate and change shape. For simplicity, the thermal conductivity values at 1 bar were used for xenon.

The presence of these (intra- and inter-granular) xenon bubbles decreased the thermal conductivity by more than 25 percent, as shown in Figure 2.6. According to Miller et al. [7], their sample (on which our simulations are based) went through a fission density of  $3.46 \times 10^{21} \text{ cm}^{-3}$ . At this fission density, Burkes and coworkers [1] found that the experimental thermal conductivity of U-10Mo reduced to almost 33 percent of its unirradiated value at 473 K. It should be noted that the real material has a three-dimensional grain boundary structure with varying levels of fission gas at each cross section, meaning our estimates of the thermal conductivity (which effectively assume rod-like inclusions rather than spheres) will be too low. Past studies [21, 45] have indicated that conductivity in the presence of inclusions is underestimated in two-dimensional models. This suggests that the measured conductivity (33% of the conductivity of the unirradiated material) may be

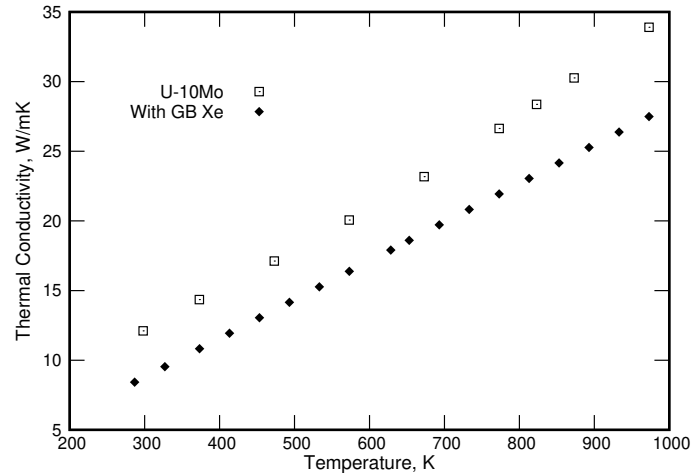


**Figure 2.6.** Comparison between the thermal conductivity of bubble-free U-10Mo with that of U-10Mo that has xenon bubbles decorating the grain boundaries according to the distribution in Figure 2.2. A 4% drop is observed, increasing with temperature.

reasonably consistent with the conductivity estimated here (i.e., 25% of the conductivity of the unirradiated material).

### 2.3.2 Effect of Xenon Pressure on the Overall Thermal Conductivity

To evaluate the impact of the pressure of the xenon bubbles on the overall thermal conductivity, we performed a study of the overall conductivity as a function of temperature for five different xenon bubble pressures given a fixed bubble distribution (Figure 2.1b). Each pressure has a distinct thermal conductivity (Figure 2.3) as a function of temperature. In this part of the study, a constant bubble size was used (radius 1.55 nm). The results are shown in Figure 2.7. The results show little to no change of the overall thermal conductivity of the fuel due to the bubbles' pressure over the range studied. However, though xenon has a wide range of thermal conductivities at different pressures (see Figure 2.3), the effect is negligible relative to the thermal conductivity of the fuel.

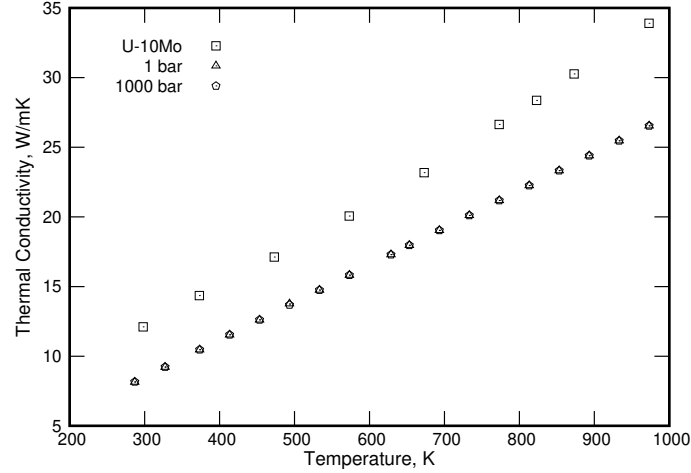


**Figure 2.7.** Overall thermal conductivity of U-10Mo using the thermal conductivity of xenon at two extremes of pressure (1 bar and 1000 bar), compared to that of pure (bubble-free) U-10Mo. Bubbles are distributed as in Figure 2.1b with radii of 1.55 nm.

### 2.3.3 Effect of Bubble Arrangement on Thermal Conductivity

We performed a series of simulations to determine whether bubble distribution has a significant influence on the overall thermal conductivity. Two cases were considered. In the first case, we used same number (16) of bubbles of the same diameter (1 nm) and organized them into five different arrangements. The arrangements are arbitrary, but each has the same area fraction of bubbles (xenon gas). In the first arrangement (Figure 2.8a), the bubbles are dispersed uniformly throughout the domain. In Figure 2.8b, the bubbles are arranged in a denser pattern with bubble-free portions near the high-temperature side. In Figure 2.8c, the bubbles are arranged in one corner. In Figure 2.8d, the bubbles are tightly clustered near the center of the domain, creating significant bubble-free regions at the top and bottom. The overall thermal conductivities for these arrangements are presented in Figure 2.9. In these simulations, heat is flowing from left to right, whereas the top and bottom boundaries are insulating (adiabatic).

Based on the results from Figure 2.8, arrangement (d) shows a minor deviation, particularly at high temperatures, compared to the other arrangements. The other four bubble

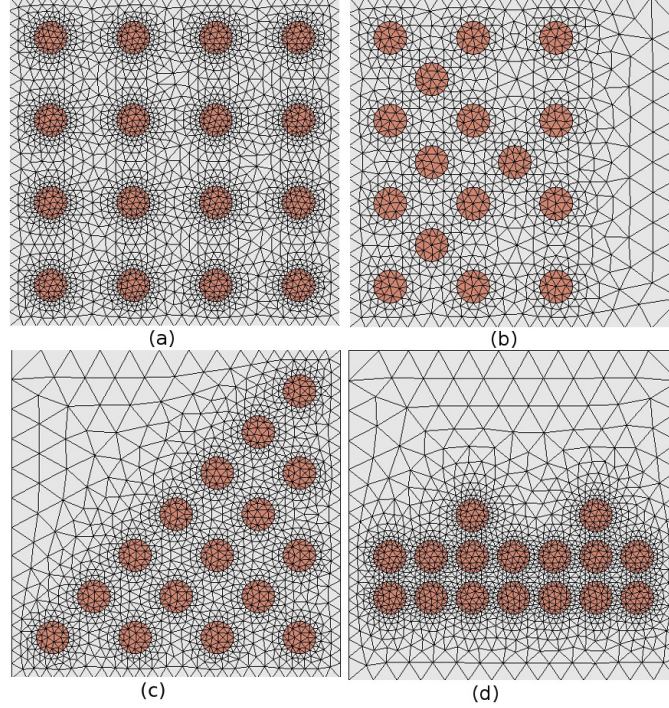


**Figure 2.8.** Different bubble arrangements in which the area of each bubble and the number of bubbles are the same. Heat flows from left to right in these simulations; only arrangement (d), with its uninterrupted “heat channel” in the top half of the domain, shows significantly different conductivity.

arrangements do not produce significantly different thermal conductivities. The reason for the deviation for case (d) is the relatively wide “heat channel” in the direction of the heat flow, which is absent in the other arrangements. The highest thermal conductivity difference between Figure 2.8d and the other arrangements is approximately  $0.93 \text{ W/m}\cdot\text{K}$ , which is also a function of the open channel’s area.

In the second case, different bubble sizes were used with constant total area. As the first case shows, bubble arrangement has minimal impact on the overall heat transfer unless it produces a significant heat transfer channel in direction of the heat flow. In this step, we kept the total area covered by the bubbles the same, but with different sizes of bubbles. To keep the area same while decreasing the bubble diameter, the number of bubbles increases. Figure 2.10 shows the four different arrangements with different bubble sizes. None of



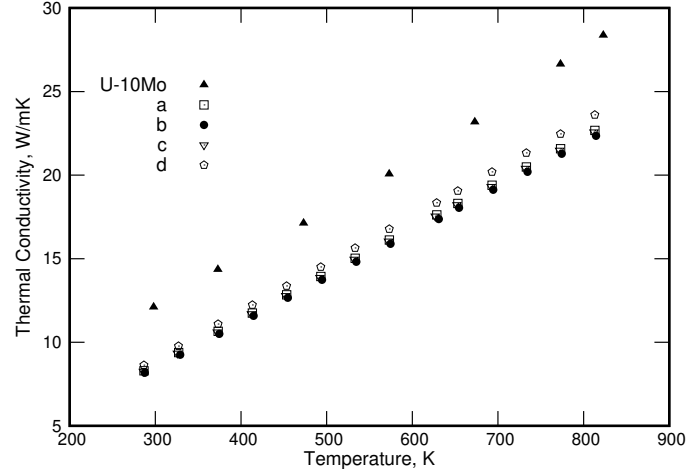


**Figure 2.9.** Comparison of the calculated thermal conductivity of different bubble arrangements (constant bubble area and diameter). Only arrangement (d), with its properly-oriented “heat channel,” shows significant differences from the others, and such differences are relatively insignificant compared to the bubble-free conductivity.

the arrangements creates a heat transfer channel in the direction of heat flow. The results are shown in Figure 2.11. The results show no significant change in the overall thermal conductivity. We conclude that the bubble arrangement has little impact unless it produces a significant bubble-free heat transfer channel.

In our calculation, grain boundary xenon gas bubbles had very minimal impact on the overall heat transfer. That is because our sample has very low grain boundary fission gas areal density, less than 2% of the total area. Grain boundary fission gas bubble size increases with an increase in burnup [5]. With an increase in fission density, more fission gas usually diffuses to the grain boundary area and recrystallization [46] subdivides the grains to accommodate the fission gas near the grain boundaries. This also increases the grain boundary fission gas density. Our results were also compared with porosity correction models, specifically those of Bauer [47] and Peddicord [48]. Bauer’s model ( $\lambda = \lambda_0 e^{(-2.14\nu)}$ , where  $\lambda_0$  is the thermal conductivity of the 100% dense material and  $\nu$  is the porosity) over-predicts the porosity correction factor for thermal conductivity. Peddicord’s model ( $\lambda = \lambda_0 (1 - \nu)^{2.58}$ ) agrees better with the effective thermal conductivity from

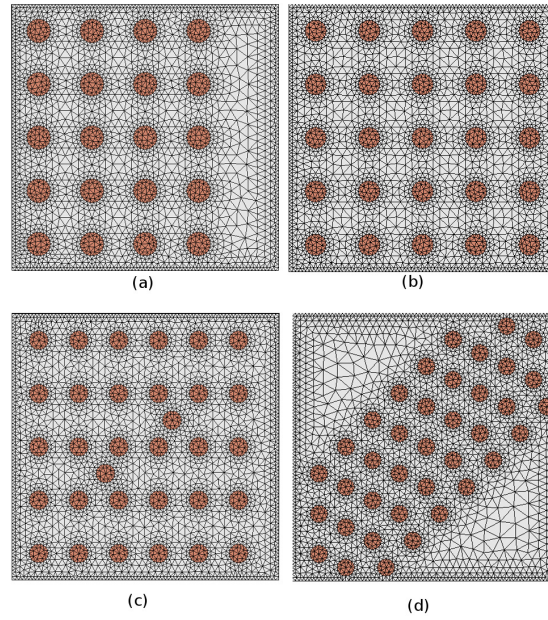


**Figure 2.10.** Different bubble arrangements where the area is the same but the bubbles have different diameters. (a) 20 bubbles, (b) 25 bubbles, (c) 32 bubbles, (d) 38 bubbles.

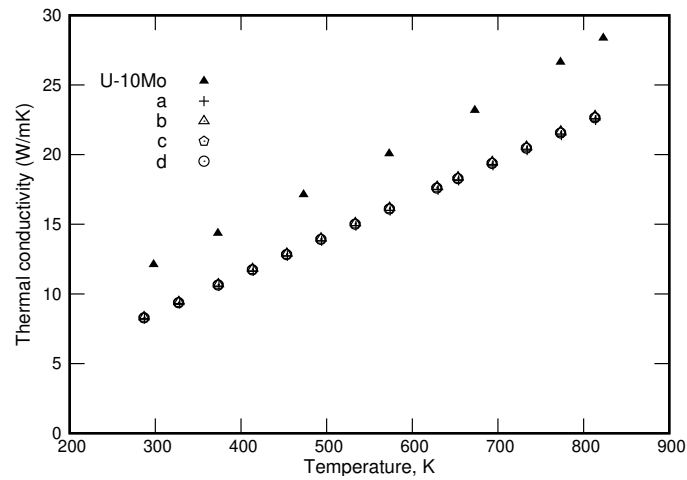


**Figure 2.11.** Comparison of thermal conductivity between different bubble diameters at constant total bubble area with bubble-free U-10Mo. Bubble arrangements are shown in Figure 2.10. Bubble diameters are (a) 0.894 nm (b) 0.8 nm (c) 0.707 nm and (d) 0.6488 nm; the bubble area fraction is 12.6% percent.

our simulations. All these empirical models are applicable to intragranular gas bubbles with uniform distribution and negligible fission gas thermal conductivity. In our calculation, all the thermal conductivities are measured from two-dimensional finite element models, but two-dimensional thermal conductivity usually represents the lower limit of the three-dimensional thermal conductivity [49]. Accurate estimation of this limit is very important.

## **2.4 Conclusions**

Estimating the thermal conductivity of nuclear fuel is an important part of understanding fuel behavior in nuclear reactors. In our work, xenon gas was used to represent fission gas bubbles in U-10Mo monolithic fuels. The impact of distributed xenon bubbles on the overall thermal conductivity of U-10Mo is significant, resulting in a 25–35 percent drop in conductivity for the bubble volume fractions studied, largely independent of bubble arrangement. Both intra- and inter-granular gas bubble structures were used. For intra-granular bubbles, a gas bubble superlattice structure was used. The results indicate that the Maxwell–Eucken and Hashin–Shtrikman models overestimate thermal conductivities by at least 5% for the bubble volume fraction studied.

The pressure dependence of xenon’s thermal conductivity was also studied to estimate the impact of bubble pressure on the overall thermal conductivity of U-10Mo. Our results indicate that bubble pressure is not a significant factor for the bubble densities studied—the overall thermal conductivity remains largely unchanged between 1 bar and 1000 bar.

We find that both intra- and inter-granular xenon bubbles reduce the overall thermal conductivity by more than 25 percent. Different bubble arrangements have very little impact on the overall heat flow, unless the arrangement leads to a significant bubble-free channel through which heat can be conducted without interference from nearby bubbles. Bubble size is also not a significant factor, as different bubble sizes at the same bubble areal density produce a U-10Mo slab with identical overall conductivity.

## References

1. Douglas E. Burkes, Andrew M. Casella, Amanda J. Casella, Edgar C. Buck, Karl N. Pool, Paul J. MacFarlan, Matthew K. Edwards, and Frances N. Smith. Thermal properties of U–Mo alloys irradiated to moderate burnup and power. *J. Nucl. Mater.*, 464:331–341, 2015.
2. Vincenzo V. Rondinella and Thierry Wiss. The high burn-up structure in nuclear fuel. *Mater. Today*, 13(12):24–32, 2010.
3. A. T. Blades, W. H. Fleming, and H. G. Thode. The ratio of xenon to krypton in  $U^{235}$  fission. *Can. J. Chem.*, 34(3):233–237, 1956.
4. J. A. Petruska, H. G. Thode, and R. H. Tomlinson. The absolute fission yields of twenty-eight mass chains in the thermal neutron fission of  $U^{235}$ . *Can. J. Phys.*, 33(11):693–706, 1955.
5. Yeon Soo Kim and G. L. Hofman. Fission product induced swelling of U–Mo alloy fuel. *J. Nucl. Mater.*, 419(1):291–301, 2011.
6. B. D. Miller, J. Gan, D. D. Keiser, Jr, A. B. Robinson, J. F. Jue, J. W. Madden, and P. G. Medvedev. Transmission electron microscopy characterization of the fission gas bubble superlattice in irradiated U–7wt% Mo dispersion fuels. *J. Nucl. Mater.*, 458:115–121, 2015.
7. Brandon D. Miller, Jian Gan, James Madden, Jan-Fong Jue, A. Robinson, and D. D. Keiser. Advantages and disadvantages of using a focused ion beam to prepare TEM samples from irradiated U–10Mo monolithic nuclear fuel. *J. Nucl. Mater.*, 424(1):38–42, 2012.
8. Jian Gan, D. D. Keiser, Dan M. Wachs, Adam B. Robinson, Brandon D. Miller, and Todd R. Allen. Transmission electron microscopy characterization of irradiated U–7Mo/Al–2Si dispersion fuel. *J. Nucl. Mater.*, 396(2):234–239, 2010.
9. Jian Gan, D. D. Keiser, Brandon D. Miller, Adam B. Robinson, Jan-Fong Jue, Pavel Medvedev, and Dan M. Wachs. TEM characterization of U–7Mo/Al–2Si dispersion fuel irradiated to intermediate and high fission densities. *J. Nucl. Mater.*, 424(1):43–50, 2012.
10. P. B. Johnson and D. J. Mazey. The gas-bubble superlattice and the development of surface structure in  $He^+$  and H irradiated metals at 300 K. *J. Nucl. Mater.*, 93–94:721–727, 1980.
11. P. B. Johnson and D. J. Mazey. Hydrogen gas-bubble structure in proton-irradiated copper at 300 K. *J. Nucl. Mater.*, 91(1):41–46, 1980.
12. J. H. Evans. Void and bubble lattice formation in molybdenum: A mechanism based on two-dimensional self-interstitial diffusion. *J. Nucl. Mater.*, 119(2–3):180–188, 1983.

13. D. J. Mazey and J. H. Evans. Bubble lattice formation in titanium injected with krypton ions. *J. Nucl. Mater.*, 138(1):16–18, 1986.
14. J. H. Evans and D. J. Mazey. Solid bubble formation in titanium injected with krypton ions. *J. Nucl. Mater.*, 138(2-3):176–184, 1986.
15. P. B. Johnson, K. J. Stevens, and R. W. Thomson. Image processing techniques in the study of ordered bubble arrays: Bubble facetting in vanadium. *Nucl. Instrum. Meth. Phys. Res. B*, 62(2):218–227, 1991.
16. P. B. Johnson and D. J. Mazey. Gas-bubble superlattice formation in bcc metals. *J. Nucl. Mater.*, 218(3):273–288, 1995.
17. F. E. Lawson and P. B. Johnson. A temperature threshold for gas-bubble superlattice formation in molybdenum. *J. Nucl. Mater.*, 252(1-2):34–42, 1998.
18. N. M. Ghoniem, Daniel Walgraef, and S. J. Zinkle. Theory and experiment of nanostructure self-organization in irradiated materials. 8(1):1–38, 2001.
19. P. B. Johnson and Fenella Lawson. Helium gas-bubble superlattice formation in molybdenum. *Nucl. Instrum. Meth. Phys. Res. B*, 243(2):325–334, 2006.
20. J. Gan, D. D. Keiser, Jr., B. D. Miller, A. B. Robinson, D. M. Wachs, and M. K. Meyer. Thermal stability of fission gas bubble superlattice in irradiated U–10Mo fuel. *J. Nucl. Mater.*, 464:1–5, September 2015.
21. K. Bakker. Using the finite element method to compute the influence of complex porosity and inclusion structures on the thermal and electrical conductivity. *Int. J. Heat Mass Tran.*, 40(15):3503–3511, 1997.
22. James Clerk Maxwell. *A Treatise on Electricity and Magnetism*, volume 1. Clarendon Press, Oxford, 1881.
23. J. B. MacEwan, R. L. Stoute, and M. J. F. Notley. Effect of porosity on the thermal conductivity of  $\text{UO}_2$ . *J. Nucl. Mater.*, 24(1):109–112, 1967.
24. L. A. Goldsmith and J. A. M. Douglas. Measurements of the thermal conductivity of uranium dioxide at 670–1270 K. *J. Nucl. Mater.*, 47(1):31–42, 1973.
25. M. F. DeVries. An experimental determination of the thermal conductivity of a 304L stainless steel powder metallurgy material. *J. Heat Tran.*, 111:281, 1989.
26. Arthur L. Loeb. Thermal conductivity: VIII, A theory of thermal conductivity of porous materials. *J. Am. Ceram. Soc.*, 37(2):96–99, 1954.
27. M. E. Cunningham and K. L. Peddicord. Heat conduction in spheres packed in an infinite regular cubical array. *Int. J. Heat Mass Tran.*, 24(7):1081–1088, 1981.
28. Da Yu Tzou. The effect of internal heat transfer in cavities on the overall thermal conductivity. *Int. J. Heat Mass Tran.*, 34(7):1839–1846, 1991.

29. T. H. Bauer. A general analytical approach toward the thermal conductivity of porous media. *Int. J. Heat Mass Tran.*, 36(17):4181–4191, 1993.
30. Shenyang Hu, Andrew M. Casella, Curt A. Lavender, David J. Senor, and Douglas E. Burkes. Assessment of effective thermal conductivity in U–Mo metallic fuels with distributed gas bubbles. *J. Nucl. Mater.*, 462:64–76, 2015.
31. Trellis Pro. Computational simulation software. csimsoft, LLC., American Fork, Utah, 2012–2017.
32. Viktor Abramovich Rabinovich, A. A. Vasserman, V. I. Nedostup, and Lo S. Veksler. *Thermophysical Properties of Neon, Argon, Krypton, and Xenon*. Hemisphere Publishing Corporation, New York, NY, 1987.
33. Albert R. Kaufmann. *Nuclear Reactor Fuel Elements: Metallurgy and Fabrication*. Interscience Publishers, New York, 1962.
34. Douglas E Burkes, Cynthia A Papesch, Andrew P Maddison, Thomas Hartmann, and Francine J Rice. Thermo-physical properties of DU–10wt.% Mo alloys. *J. Nucl. Mater.*, 403(1):160–166, 2010.
35. G. W. Greenwood, A. J. E. Foreman, and D. E. Rimmer. The role of vacancies and dislocations in the nucleation and growth of gas bubbles in irradiated fissile material. *J. Nucl. Mater.*, 1(4):305–324, 1959.
36. H. Trinkaus. Energetics and formation kinetics of helium bubbles in metals. *Radiat. Eff.*, 78(1–4):189–211, 1983.
37. Hongxing Xiao, Chongsheng Long, Xiaofeng Tian, and Shujian Li. Atomistic simulations of the small xenon bubble behavior in U–Mo alloy. *Mater. Des.*, 74:55–60, 2015.
38. L. E. Thomas. Condensed-phase xenon and krypton in UO<sub>2</sub> spent fuel. In *Fundamental Aspects of Inert Gases in Solids*, pages 431–441. Springer, New York, 1991.
39. M. Ross and A. K. McMahan. Condensed xenon at high pressure. *Phys. Rev. B*, 21(4):1658–1664, 1980.
40. J. Zheng, Q. F. Chen, Y. J. Gu, Z. Y. Chen, and C. J. Li. Thermodynamics, compressibility, and phase diagram: Shock compression of supercritical fluid xenon. *J. Chem. Phys.*, 141(12):124, 2014.
41. Derek Gaston, Chris Newman, Glen Hansen, and Damien Lebrun-Grandie. MOOSE: A parallel computational framework for coupled systems of nonlinear equations. *Nucl. Eng. Des.*, 239(10):1768–1778, 2009.
42. C. R. Clark, G. C. Knighton, M. K. Meyer, and G. L. Hofman. Monolithic fuel plate development at Argonne National Laboratory. In *2003 International Meeting on Reduced Enrichment for Research and Test Reactors*, volume 1, Chicago, Illinois, October 2003.

43. David S. Smith, Arnaud Alzina, Julie Bourret, Benoît Nait-Ali, Fabienne Pennec, Nicolas Tessier-Doyen, Kodai Otsu, Hideaki Matsubara, Pierre Elser, and Urs. T. Gonzenbach. Thermal conductivity of porous materials. *J. Mater. Res.*, 28(17):2260–2272, 2013.
44. Zvi Hashin and Shmuel Shtrikman. A variational approach to the theory of the effective magnetic permeability of multiphase materials. *J. Appl. Phys.*, 33(10):3125–3131, 1962.
45. Brigitte Schulz. Thermal conductivity of porous and highly porous. *High Temp. High Press.*, 13:649–660, 1981.
46. Yeon Soo Kim, G.L. Hofman, and J. S. Cheon. Recrystallization and fission-gas-bubble swelling of U–Mo fuel. *J. Nucl. Mater.*, 436(1):14–22, 2013.
47. Theodore H. Bauer and John W. Holland. In-pile measurement of the thermal conductivity of irradiated metallic fuel. *Nucl. Technol.*, 110(3):407–421, 1995.
48. K. L. Peddicord, M. E. Cunningham, and A Tripathi. Porosity correction to thermal conductivity based on analytical temperature solutions. *Trans. Am. Nucl. Soc.*, 28:548, 1978.
49. K. Bakker, H. Kwast, and E. H. P. Cordfunke. Determination of a porosity correction factor for the thermal conductivity of irradiated  $\text{UO}_2$  fuel by means of the finite element method. *J. Nucl. Mater.*, 226(1–2):128–143, 1995.

## CHAPTER 3

### FIRST-PRINCIPLES STUDY OF METALLIC URANIUM

#### 3.1 Introduction

Uranium is the heaviest naturally-occurring element on Earth. The discovery of fission in uranium (specifically, in  $^{235}\text{U}$ ) impacted not only scientists and engineers all over the world, it also changed global politics forever. In nuclear research, the nucleus of the uranium atom is of much more importance than the electrons surrounding it, but the electronic structure is important to the thermodynamic properties, including crystal structure. The structural features are particularly important to the study of next-generation nuclear fuels, such as U-10Mo, that are based on metallic uranium. The electronic behavior of uranium, along with other light actinides (Pa–Pu), results in a low-symmetry crystal structure at ambient temperature and pressure—most metallic elements take on relatively high-symmetry structures (bcc, fcc, and hcp), but the light actinides are either orthorhombic or monoclinic at standard temperature and pressure. Pure uranium exists in three different solid phases at atmospheric pressure, depending on the temperature:  $\alpha$  (base-centered orthorhombic),  $\beta$  (tetragonal) and  $\gamma$  (body-centered cubic). At atmospheric pressure,  $\alpha$ -U transforms to  $\beta$ -U at approximately 935 K, and  $\beta$ -U transforms to  $\gamma$ -U at approximately 1045 K [1, 2]. The influence of  $5f$  electron–electron correlation plays a pivotal role in the crystallographic behavior of uranium and other light actinides [3, 4]; with this in mind, proper representation of uranium’s  $5f$  electrons is very important.

The stability of the crystal structures of the inner transition metals has been the target of several electronic structure studies. Eriksson and coworkers [5, 6] performed com-



parative studies of thorium, protactinium, and uranium’s crystal structures, calculating the equilibrium volume and bulk modulus using the full-potential linear-muffin-tin-orbital (FP-LMTO) technique and the local density approximation (LDA). The calculated lattice parameters and equilibrium unit cell volumes showed good agreement with experiments; the bulk modulus of protactinium was significantly underestimated, but the values for uranium and thorium were within the range of experimental values. Crocombette *et al.* [7] used norm-conserving pseudopotentials to study three metallic phases of uranium ( $\alpha$ ,  $\gamma$ , and a hypothetical fcc structure). The calculated equilibrium volume for  $\alpha$  uranium was underestimated by more than 6 percent. Söderlind [8] calculated the equilibrium lattice parameters and also estimated the elastic moduli of  $\alpha$  uranium using the FP-LMTO method. The calculated equilibrium lattice parameters were in good agreement with experimental values, but the elastic moduli did not agree particularly well with experimental values. The calculated elastic moduli were likely higher than experimental values because uranium undergoes strong phonon softening with increases in temperature, and the experimental values (taken at room temperature) would likely be lower than they would be at low temperatures [9].

Söderlind’s [8] was the first attempt to calculate  $\alpha$ -uranium’s elastic moduli. Other theoretical studies of light actinides prior to 2000 using full-core (*i.e.*, non-pseudopotential-based) techniques are summarized by Jones *et al.* [10]. Taylor [11] studied uranium phases using the projector augmented-wave (PAW) method [12] with Perdew and Wang’s 1991 (PW91) exchange–correlation functional [13, 14]. Taylor investigated  $\alpha$ , bcc, and fcc uranium. The equilibrium lattice parameters of  $\alpha$ -uranium were within 1% of experimental values at 50 K [15]. The lattice parameter of  $\gamma$ -uranium was also in good agreement with experimental values, though the lattice parameter of fcc uranium was overestimated compared to the value calculated by Crocombette *et al.* [7]. Xiang *et al.* [16] used the Perdew–Burke–Ernzerhof (PBE) exchange–correlation functional [17, 18] to study the equilibrium volume of the  $\alpha$  and  $\gamma$  uranium. He also studied the bct structure, an approximation of the  $\beta$  phase. Their results were also in good agreement with previous full potential studies and

experimental results. Li *et al.* [19] also studied the structure, formation energies, and elastic moduli of  $\alpha$ ,  $\beta$ ,  $\gamma$ , fcc, and hcp uranium using the PW91 exchange–correlation functional. Their pseudopotential produced reasonably accurate lattice parameters and cell volumes for  $\gamma$ -uranium and  $\alpha$ -uranium accompanied by reasonable elastic moduli. Beeler *et al.* [20] utilized the PBE exchange–correlation functional to study uranium, and found similar values to Li *et al.*, with the exception of the body-centered tetragonal case (approximating  $\beta$ -uranium).

In the present work, we investigate the crystal structure and elastic properties of metallic uranium with density functional theory (DFT) with a projector augmented wave (PAW) pseudopotential [12]. We investigate four structures of uranium:  $\alpha$ ,  $\gamma$ , bct, and fcc. Our results are compared with previously published electronic structure calculations and experiments. The electronic densities of states for all four crystal structures are also calculated. Our results for  $\alpha$ -uranium are comparable to previous models, but predicted properties for  $\gamma$ -uranium are, in general, improvements on previously-published models.

### 3.2 Density Functional Theory: A Brief Introduction

Modern first-principles electronic structure calculations in solids are based on the density functional theorem (DFT) of P. Hohenberg and W. Kohn (1964) [21]. It states that the total energy,  $E$ , of a non-spin-polarized system of interacting electrons in an external potential (i.e Coulomb potential due to the nuclei in a solid) is exactly a functional of the ground state electronic density,  $\rho$ .

$$E = E[\rho] \tag{3.1}$$

It also showed that the true ground state density is the density that minimizes  $E[\rho]$ , and the other ground state properties are also functionals of the ground state. Before Hohenberg and Kohn (H-K), the original density functional theory of quantum system is the method of Thomas [22] and Fermi [23] proposed in 1927. In the Thomas-Fermi method the kinetic

energy of the system electrons is approximated as an explicit functional of the density. This model fails to explain some of the useful description of the electrons in matter.

Even though original paper only talked about non-spin-polarized system, the extension to spin-polarized systems is straightforward. The  $E$  and other ground state properties become functionals of the spin density. In a simple collinear case, where the spin-up and spin-down densities are enough, then the ground state would be :

$$E = E[\rho_{\uparrow}, \rho_{\downarrow}] \quad (3.2)$$

The H-K theorem does not provide any guidance how to achieve  $E[\rho]$ , and the usefulness of DFT depends on the proper approximation of the functional. To approach this challenge, the unknown functional,  $E[\rho]$ , is written as the Hartree total energy plus another, but presumably smaller, unknown functional, called the exchange-correlation (xc) functional,  $E_{xc}[\rho]$ .

$$E[\rho] = T_s[\rho] + E_{ei}[\rho] + E_H[\rho] + E_{ii}[\rho] + E_{xc}[\rho] \quad (3.3)$$

Here  $T_s[\rho]$  denotes the single particle kinetic energy,  $E_{ei}[\rho]$  is the Coulomb interaction energy between the electrons and the nuclei,  $E_{ii}[\rho]$  arises from the interaction between the nuclei with each other, and  $E_H[\rho]$  is Hartree component of the electron-electron energy,

$$E_H[\rho] = \frac{e^2}{2} \int d^3\mathbf{r} d^3\mathbf{r}' \frac{\rho(\mathbf{r})\rho(\mathbf{r}')}{|\mathbf{r} - \mathbf{r}'|} \quad (3.4)$$

$E_{xc}[\rho]$  is an unknown functional. Several useful approximations are made for this particular functional. The simplest is the local density approximation (LDA). In the LDA,  $E_{xc}[\rho]$  is written as

$$E_{xc}[\rho] = \int d^3\mathbf{r} \rho(\mathbf{r}) \epsilon_{xc}(\rho(\mathbf{r})) \quad (3.5)$$

Where  $\epsilon_{xc}$  is approximated by a local function of the density, usually that which reproduces the known energy of the uniform electron gas. The other commonly used approximations

are the generalized gradient approximations (GGAs), where the local gradient as well as the density is used in order to incorporate more information about the electron gas ( $\epsilon_{xc}(\rho)$  is replaced by  $\epsilon_{xc}(\rho, |\nabla\rho|)$ ). The relation between the different approximations can be understood using the exact expression for the exchange correlation energy in terms of pair correlation function [24].

Kohn and Sham [25] wrote the electron density as a sum of single particle densities, and used the variational property to find a way to calculate the ground state energy and density, given the functional  $E_{xc}$ . More precisely, they showed that the correct density is given by the self-consistent solution of a set of single particle Schrödinger -like equations, known as Kohn-Sham (KS) equation, with a dependent potential,

$$\{T + V_{ei}(\mathbf{r}) + V_H(\mathbf{r}) + V_{xc}(\mathbf{r})\}\varphi_i(\mathbf{r}) = \epsilon_i\varphi_i(\mathbf{r}) \quad (3.6)$$

Where the density is given by a Fermi sum over the occupied orbitals,

$$\rho(\mathbf{r}) = \sum_{occ} \varphi_i^*(\mathbf{r})\varphi_i(\mathbf{r}) \quad (3.7)$$

Here the highest occupied orbital is determined by the electron count, the  $\varphi_i$  are the single particle K-S orbitals, the  $\epsilon_i$  are the corresponding K-S eigenvalues,  $T$  is the single particle kinetic energy operator,  $V_{ie}$  is the Coulomb potential due to the nuclei,  $V_H$  is the Hartree potential and  $V_{xc}$  is the exchange correlation potential. Both  $V_{xc}$  and  $V_H$  depend on  $\rho$ .

$$V_H(\mathbf{r}) = e^2 \int d^3\mathbf{r}' \frac{\rho(\mathbf{r}')}{|\mathbf{r} - \mathbf{r}'|} \quad (3.8)$$

$$V_{xc}(\mathbf{r}) = \frac{\delta E_{xc}[\rho]}{\delta \rho(\mathbf{r})} \quad (3.9)$$

In this framework, a calculation entails the self-consistent solutions of Eqn 3.6 and 3.7. Which usually means, a density must be found such that it yields an effective potential that

when inserted into the Schrödinger -like equations yields orbitals that reproduces it. In this way, instead of solving a many-body Schrödinger equation using DFT, the problem is now solving a series of single particle equations, with the requirement of self-consistency. This leads to a wide variety of technique regarding DFT. The plane-wave expansion of K-S orbitals are widely used in codes like QuantumEspresso [26] and Abinit [27]. The method to use a basis to represent the KS orbitals are:

$$\varphi_i(\mathbf{r}) = \sum_{\alpha} c_{i\alpha} \phi_{\alpha}(\mathbf{r}) \quad (3.10)$$

Where the  $\phi_{\alpha}(\mathbf{r})$  are the basis functions and the  $C_{i\alpha}$  are expansion coefficients.

### 3.2.1 Solution of the Single particle Kohn-Sham Equations

The previous section addressed the formation of K-S equation and the idea of self-consistency. In DFT based calculation, methods are classified based on the representation of the density, potential and especially KS orbitals. The choice of representation is made to increase the computational efficiency, while maintaining the accuracy. For a choice of basis, the coefficients are the only variable to be determined (density depends on KS orbitals). The total energy of DFT becomes variational, then the solution of the self-consistent KS equations requires to determine the  $C_{i\alpha}$  for the occupied orbitals that provides a minima of the total energy.

According to the second theorem of Hohenberg and Kohn, all properties such as kinetic energy, etc. are uniquely determined if  $\rho(\mathbf{r})$  is specified. Eqn 3.6 shows the relationship. To minimize the total energy with respect of KS orbitals, the variational principle is usually used. While performing the minimization, it is prefer to minimize with  $\varphi^*(\mathbf{r})$  (both yield the same result). Using the chain rule for functional derivatives, the equations becomes:

$$\frac{\delta E}{\delta \varphi_i^*(\mathbf{r})} = \frac{\delta T_s}{\delta \varphi_i^*(\mathbf{r})} + \left[ \frac{\delta E_{ext}}{\delta \varphi_i^*(\mathbf{r})} + \frac{\delta E_H}{\delta \varphi_i^*(\mathbf{r})} + \frac{E_{xc}}{\delta \varphi_i^*(\mathbf{r})} \right] \frac{\delta \rho(\mathbf{r})}{\delta \varphi_i^*(\mathbf{r})} = 0 \quad (3.11)$$

The kinetic energy may be differentiated separated with respect to orbital. In the above equation the  $E_{ei}$  is replaced with  $E_{ext}$  which means potential due to nuclei and any other external fields.

$$-\frac{1}{2}\nabla^2\varphi_i^*(\mathbf{r}) + \left[ V_{ext}(\mathbf{r}) + \int d(\mathbf{r}') \frac{\rho(\mathbf{r}')}{|\mathbf{r} - \mathbf{r}'|} + \epsilon_{xc}(\rho) + \rho(\mathbf{r}) \frac{\delta\epsilon_{xc}[\rho]}{\delta\rho(\mathbf{r})} \right] \varphi_i(\mathbf{r}) = \epsilon_i \varphi_i(\mathbf{r}) \quad (3.12)$$

Eqn 3.12 is a system of equations, represent the many-particle system in terms of single-particle orbitals. Each of these equations resemble a Schrödinger equation

$$\left[ \hat{T} + V_{eff} \right] \varphi_i(\mathbf{r}) = \epsilon_i \varphi_i(\mathbf{r}) \quad (3.13)$$

Deriving Eqn 3.12 from Eqn 3.11 involves variational principle and using Lagrange multiplier for Schrödinger equation. Here the  $V_{eff}$  is the sum of the  $V_H$ ,  $V_{xc}$  and  $V_{ext}$ , which depends on the density and indirectly depends on orbitals. Now we have an equation where any change in the orbitals effect also the potential on which they in turn depend on orbital. This problem is resolved by solving Kohn-Sham system of equations self-consistently.

### 3.3 Kohn-Sham problem for an isolated atom

For an one-electron atom, the Coulombic potential,  $V(\mathbf{r}) = V(r) = -Z/r$  is spherically symmetric, the solution can be split into a radial and an angular part

$$\psi_{nlm}(\mathbf{r}) = \psi_{nl}(r)Y_{lm}(\theta, \phi) = r^{-1}\phi_{nl}(r)Y_{lm}(\theta, \phi) \quad (3.14)$$

The above equation sometime is referred to as spherically symmetric Schrödinger equation and  $Y_{lm}(\theta, \phi)$  are normalized spherical harmonics. Using the Laplacian in the spherical coordinates the wave equation can be reduced to the radial equation for principle quantum

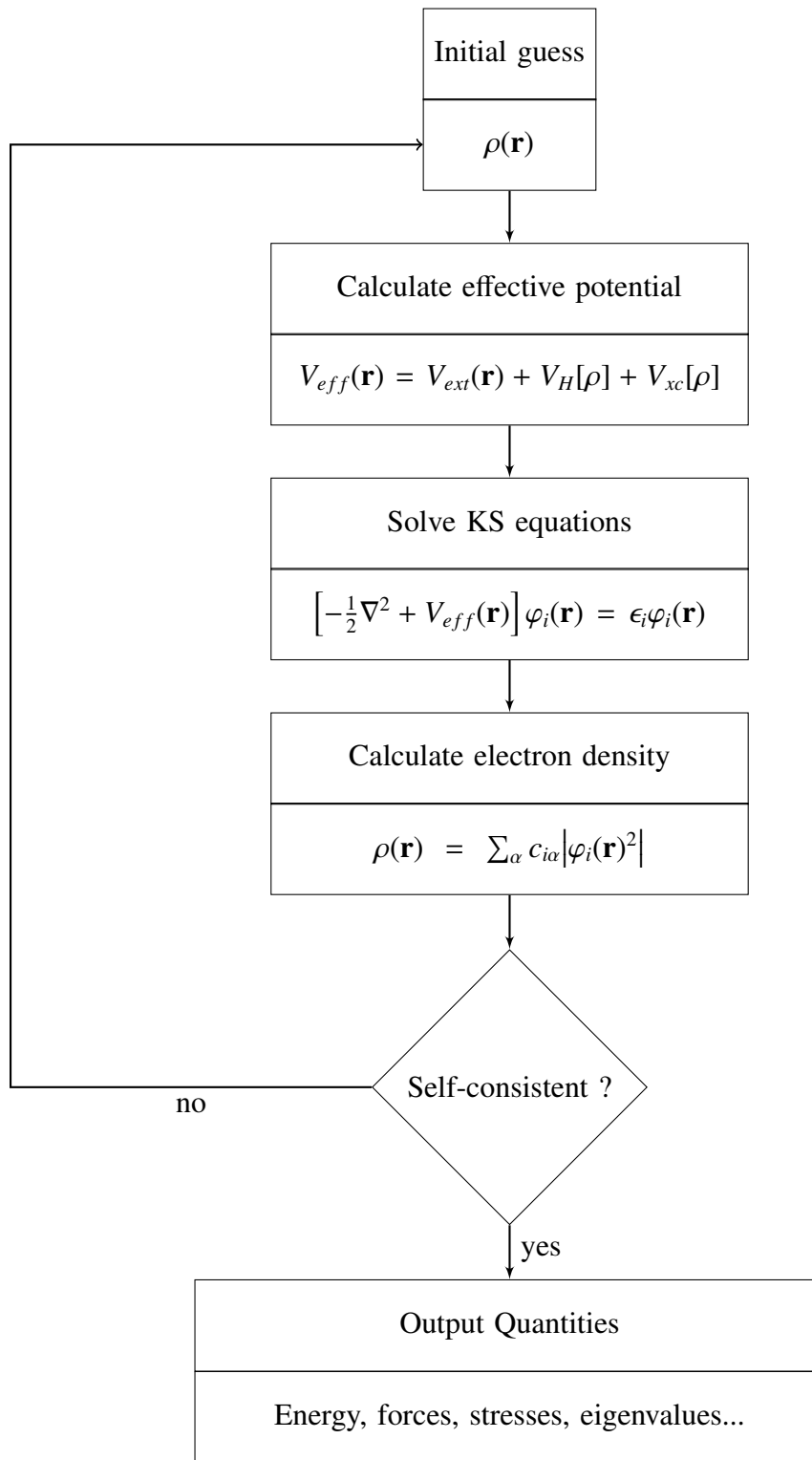


**Figure 3.1.** Schematic representation of the self-consistent loop solution of Kohn-Sham equations.

number  $n$

$$-\frac{1}{2} \frac{d^2}{dr^2} \psi_{nl} + \left[ \frac{l(l+1)}{2r^2} + V_{ext}(r) - \epsilon_{nl} \right] \psi_{nl} = 0 \quad (3.15)$$

In the Kohn-Sham approach to the many-particle system, the form of the single-particle equations are identical to the above radial Schrödinger equation with an effective potential  $V_{eff}$  replacing the Coulomb potential. The effective potential ( $V_{eff} = V_{ext}(r) + V_H(r) + V_{xc}(r)$ ) is spherically symmetric in the Kohn-Sham approach. The independent-particle Kohn-Sham states may be classified by the angular quantum numbers  $L = \{l, m\}$ , and the one particle equations becomes analogous to the Schrödinger equation for one-electron atom.

$$-\frac{1}{2} \frac{d^2}{dr^2} \psi_{nl} + \left[ \frac{l(l+1)}{2r^2} + V_{eff}(r) - \epsilon_{nl} \right] \psi_{nl} = 0 \quad (3.16)$$

### 3.4 Theory of Pseudopotential

In Solids, the electrons and nuclei interact strongly through the Coulomb potential. However, according to the Fermi Liquid theory (FLT) the electronic excitation near the Fermi energy in metals behave as if they were independent particles. This leaves the strong interactions with the core electrons and the nuclei. In most cases, the core electrons are quite strongly bound, and do not respond effectively to the motions of the valence electrons. Hence, they can be regarded as essentially fixed. This is the essence of the pseudopotential approximation, the strong core potential is replaced by a pseudopotential, whose ground state wave function resembles the all electron wavefunction outside a selected core radius. In this way both the core states and the wiggles (Fig. 3.2) in the valance wavefunctions are removed. For many metals the pseudowavefunctions can be represented by lower number of planewaves. Thus making planewaves a simple and reasonable efficient basis for the pseudo wavefunctions.



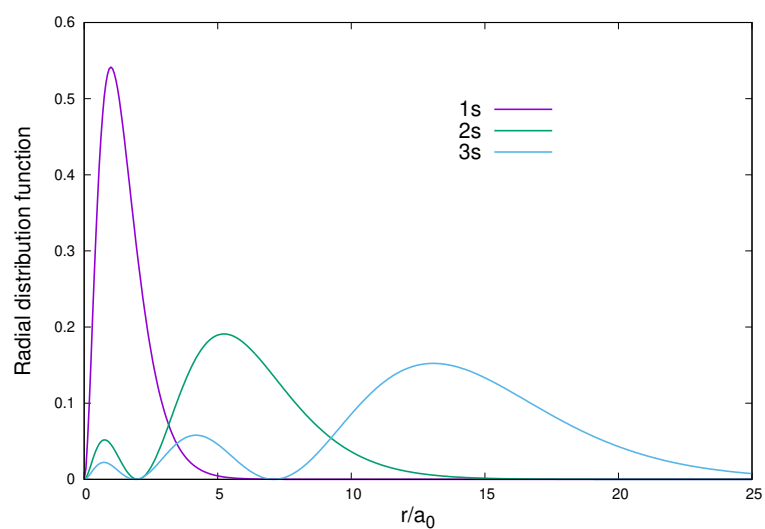


**Figure 3.2.** Radial distribution function of Hydrogenic 1s, 2s and 3s electron. It shows higher kinetic energy near the nucleus.

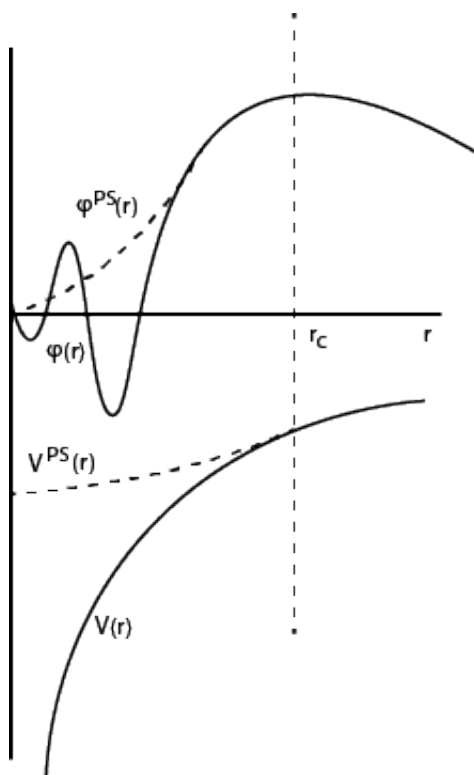


**Figure 3.3.** Schematic diagram of the replacement of all-electron wave function and core potential by a pseudo-wavefunction and pseudopotential.

### 3.4.1 Basic Phillips-Kleinman Construction

For a given many electron Hamiltonian,  $\hat{H} = \hat{T} + \hat{U}$ , where  $\hat{T}$  is the kinetic energy operator and  $\hat{U}$  is the potential energy operator, the core electron wave functions are defined by the Schrödinger equation

$$\hat{H} |\psi_i\rangle = \epsilon_i |\psi_i\rangle \quad (i = 1, ncore) \quad (3.17)$$

The valance electron wave function similarly can be found by the Hamiltonian

$$\hat{H} |\psi_v\rangle = \epsilon_v |\psi_v\rangle \quad (3.18)$$

The valence electron wave function is orthogonal to the core electron wave function ( $\langle \psi_v | \psi_i \rangle = 0$ ), this orthogonality always has to be preserved, even if the core electrons are not treated explicitly. One way to preserve this orthogonality is to write valence electron wave function in a basis set that is priori orthogonal to the core electrons. The simple Gram-Schmidt orthogonalization technique can be used. Herring [28] was the first one to use Orthogonalized plane waves (OPWs) as basis for the first quantitative calculations of bands. Using this idea, we can orthogonalize any arbitrary basis set  $\{|\chi_n\rangle\}$  to the core electron wave functions by defining a new basis set  $\{|\varrho_n\rangle\}$

$$|\varrho_n\rangle = |\chi_n\rangle - \sum_{i=1}^{ncore} \langle \psi_i | \chi_n \rangle |\psi_i\rangle \quad (3.19)$$

Here each of the new basis set,  $\{|\varrho_n\rangle\}$ , satisfies  $\langle \chi_n | \psi_i \rangle = 0$  for each  $|\psi_i\rangle$ . Now we can express the valance electron wave function as a linear combination of the new basis sets,

$$|\psi_v\rangle = \sum_n C_n |\varrho_n\rangle \quad (3.20)$$

Using Eqn 3.19 into the Eqn 3.20, the valence electron can be expressed in the following way. The orthogonality condition with the core electron still valid.

$$|\psi_v\rangle = \sum_n C_n \left[ |\chi_n\rangle - \sum_{i=1}^{ncore} |\psi_i\rangle \langle \psi_i | \chi_n \rangle \right] = |\phi\rangle - \hat{\Omega} |\phi\rangle \quad (3.21)$$

Here,  $\hat{\Omega}$  is a projection operator for core electron wave function

$$\hat{\Omega} = \sum_{i=1}^{ncore} |\psi_i\rangle \langle \psi_i| \quad (3.22)$$

and a new wave function which is a linear combination of  $|\chi_n\rangle$ , sometime designated as pseudo-orbital,

$$|\phi\rangle = \sum_n C_n |\chi_n\rangle \quad (3.23)$$

This technique of representing the valence electron wave function in preorthogonalized basis set has been studied and used as a computational tool [28]. It took the insight of the Phillips and Kleinman [29]. The new pseudoorbitals satisfies the orthogonality condition, but it also change the Hamiltonian so that the eigen values are same with the valence electrons. Mathematically, it can be obtained by replacing original valence electron Hamiltonian equation (Eqn 3.18) with newly obtained pseudo wave function.

$$\hat{H} |\psi_v\rangle = \hat{H} \left[ |\phi\rangle - \sum_n |\psi_i\rangle \langle \psi_i | \phi \rangle \right] = \epsilon_v \left[ |\phi\rangle - \sum_n |\psi_i\rangle \langle \psi_i | \phi \rangle \right] \quad (3.24)$$

Rearranging the above equation provides a new Hamiltonian,

$$\left[ \hat{H} + \sum_n^{ncore} (\epsilon_v - \epsilon_i) |\psi_i\rangle \langle \psi_i| \right] |\phi\rangle = \epsilon_v |\phi\rangle \quad (3.25)$$

The above equation has the form of the original valence electron eigenequation (3.18), but with an extra term for preorthogonalization. This extra potential ( $V_{nl} = \sum_n^{core} |\psi_i\rangle \langle \psi_i|$ ), is a nonlocal operator, and the pseudo orbital ( $|\phi\rangle$ ) is an eigenstate of the new effective

Hamiltonian,  $\hat{H} + V_{nl}$ . The new Hamiltonian has an extra potential  $V_{nl}$ , which depends on the angular momentum  $l$  due to the spherical symmetry. Because of its spherical symmetry, each angular momentum  $l, m$  can be treated separately. The dependence on  $l$  means that, a pseudopotential is an non-local operator, can be written in “semilocal” (SL) form

$$\hat{V}_{SL} = \sum_{lm} |Y_{lm}\rangle V_l(r) \langle Y_{lm}| \quad (3.26)$$

Where  $Y_{lm}(\theta, \phi) = P_l(\cos(\theta))e^{im\theta}$ . It is semi-local because it is non local on the angular variables but local in the radial variable.<sup>1</sup>

The sophistication and accuracy have evolved considerably since the Phillips-Kleinman construction. This development produces many methods of generating pseudopotentials. All of these methods follow these goals: (1) Pseudopotential should be as soft as possible, so that it can allow representation of pseudo-wavefunction with fewer planewaves. (2) Transferability has to be maintained (it means a generated pseudopotential with a configuration should produce other properties accurately) (3) the pseudo-charge density should produce the valance charge density as accurately as possible. Hamann, Schlüter and Chiang [30] developed the concept of norm-conservation, which was a first step to fulfill all the above requirements. Troullier and Martins [31] developed a more effective method to generate norm-conserving pseudopotentials for practical calculations. The projector augmented method (PAW) [12, 32] is a general approach to the solution of the first principle electronic structure problem. It introduces projectors and auxiliary localized functions. PAW preserves the all-electrons wavefunctions while keeping the pseudopotential approach. In PAW the all electron KS wavefunction is replaced by smooth pseudo wave function and auxiliary wave function. A comprehensive description of PAW formalism can be found in Blöchl’s famous paper [12].

---

<sup>1</sup> $P_l$  is the Legendre polynomials

### 3.5 Computational Details

We perform all calculations using density functional theory (DFT) with plane-wave basis sets as implemented in the software QUANTUMESPRESSO [26]. We generated a uranium pseudopotential for use with the Perdew–Burke–Ernzerhof (PBE) exchange–correlation functional [17, 18]. The projector augmented wave (PAW) pseudopotential-generating software atompaw [33, 34] was used to generate the PAW pseudopotential for uranium. The same pseudopotential was used for all subsequent calculations.

One of the major challenges in studying actinides using DFT is how to treat the large number of electrons. The pseudopotential approach effectively reduces the number of electrons by modeling the “core” as a potential energy surface, so generating a pseudopotential requires one to choose the number of electrons that will be treated explicitly. There are two approaches common for uranium: “small-core” pseudopotentials and “large-core” pseudopotentials. In a large-core pseudopotential, the valence electrons are the  $5f$ ,  $6s$ ,  $6p$ ,  $6d$  and  $7s$  shells (14 electrons). In small-core pseudopotentials, the  $5s$ ,  $5p$ , and  $5d$  shells are also included, which treats 32 electrons as valence electrons. Iche-Tarrat and Marsden [35] have discussed this topic and shown that the explicit treatment of 32 electrons only marginally improves the performance of DFT at significantly higher computational cost. The valence electron configuration of uranium used when generating our pseudopotential was  $6s^2 6p^6 7s^2 6d^1 5f^3$  (*i.e.*, it is a large-core pseudopotential). The radius of the augmentation region was chosen to be 2.5 bohr, which we determined by starting from half the experimental nearest-neighbor interatomic distance in  $\alpha$ -uranium and adjusting based on energy–volume minimization. The pseudo-partial waves were generated using the RKKJ scheme [36], which uses a sum of Bessel functions to represent the pseudo-partial waves. A plane-wave cutoff energy analysis was performed and a 50 Ry energy cutoff was found to be sufficient based on a plot of total energy against cutoff energy. All calculations were performed on primitive cells using the cell geometries and coordinates given by Crocombette *et al.* [7] for  $\alpha$ -uranium, Beeler *et al.* [20] for bct uranium, and values from the Structure

**Table 3.1.** Parameters used to generate the pseudopotential in atompaw [33, 34].

Cutoff	Value (bohr)
$r_{\text{PAW}}$	2.50
$r_{\text{shape}}$	2.02
$r_{\text{vloc}}$	1.50
$r_{\text{core}}$	1.80
$r_{c,i}$	$r_{\text{PAW}}$
EXCEPT	
$r_{c,6s}$	1.50
$r_{c,7s}$	1.50

of Crystals database [37] for all other structures. Periodic boundaries were applied in all directions. The Monkhorst–Pack scheme [38] was used for Brillouin zone sampling; the  $k$ -point meshes were  $20 \times 20 \times 26$ ,  $20 \times 20 \times 20$ ,  $18 \times 18 \times 18$ , and  $20 \times 20 \times 20$  for the  $\alpha$ , bct,  $\gamma$ , and fcc lattices, respectively. A Methfessel–Paxton [39] smearing method (width 0.02 Ry) was used to integrate the bands at the Fermi level. To calculate the nine unique elastic moduli of orthorhombic  $\alpha$ -U, the energy–strain relationship (see appendix A) was used as described by Ravindran *et al.* [40]. For cubic structures, the elastic moduli were evaluated using volume-conserving orthorhombic and monoclinic distortions as described by Beckstein *et al.* [41].

### 3.6 Results

The pseudopotential itself is generated by atompaw [33, 34], which takes as input the augmentation radius ( $r_{\text{PAW}}$ ), core radius ( $r_{\text{core}}$ ), shape function cutoff ( $r_{\text{shape}}$ ), matching radius ( $r_{\text{vloc}}$ ), valence and core electron configurations, density functional, and the cutoff radii for each of the partial waves ( $r_{c,i}$ ). We assumed  $r_c = r_{\text{PAW}}$  for all valence electrons except the 6s and 7s electrons, for which  $r_c$  was adjusted. The cutoff radii are given in Table 3.1. These cutoffs, combined with the choice of density functional and valence electrons, are sufficient to reproduce the pseudopotential in atompaw.

Properties of several uranium phases as calculated with the pseudopotential presented above are detailed in the rest of this section.

### 3.6.1 $\alpha$ -Uranium

Uranium's  $\alpha$  phase has a base-centered orthorhombic structure with space group  $Cmcm$  (no. 63). The asymmetric unit has uranium atoms at Wyckoff position  $4c \left(0, \pm y, \pm \frac{1}{4}\right)$ , where the position parameter  $y$  has been found to be a function of temperature [15]. At room temperature, the value of  $y$  has been measured to be 0.1024 [15, 42]. There are four atoms in the standard unit cell (two in the primitive cell). The  $\alpha$  phase is thermodynamically favorable at temperatures below 935 K and pressures up to 100 GPa [43, 2]. This makes the  $\alpha$  phase important to the nuclear energy community because it is the naturally-occurring phase of uranium. The solid-state physics community also shows interest in  $\alpha$ -uranium because of certain unusual characteristics, including charge density wave transitions and superconductivity.

The total energy as a function of unit cell volume for  $\alpha$  uranium is shown in Figure 3.4; Table 3.2 summarizes the optimized lattice parameters, the distance parameter  $y$ , and the calculated elastic moduli, along with results from previously published calculations and experiments. We confirm that  $\alpha$ -U is the lowest-energy crystal structure among those we tested. Our pseudopotential predicts an equilibrium volume of  $20.49 \text{ \AA}^3$ , which is in close agreement with the experimental value of  $20.530 \text{ \AA}^3$  (at 50 K). The position parameter  $y$  exhibits a minimum-energy value of 0.0986 at the equilibrium volume of  $20.49 \text{ \AA}^3$ . This trend in  $y$  is similar to that observed in the calculations of Wills and Eriksson [5].

Our cell volume results differ from previous calculations using PAW [20], which obtained an equilibrium volume of  $19.987 \text{ \AA}^3$ . A Murnaghan [44] fit to the total energy as a function of volume for  $\alpha$ -uranium yielded a bulk modulus of 132.1 GPa, which is larger than the experimental value of  $104 \pm 2 \text{ GPa}$  [43], but agrees closely with the quantum molecular dynamics (QMD) results of Hood *et al.* [45] (133.5 GPa) and the diamond anvil

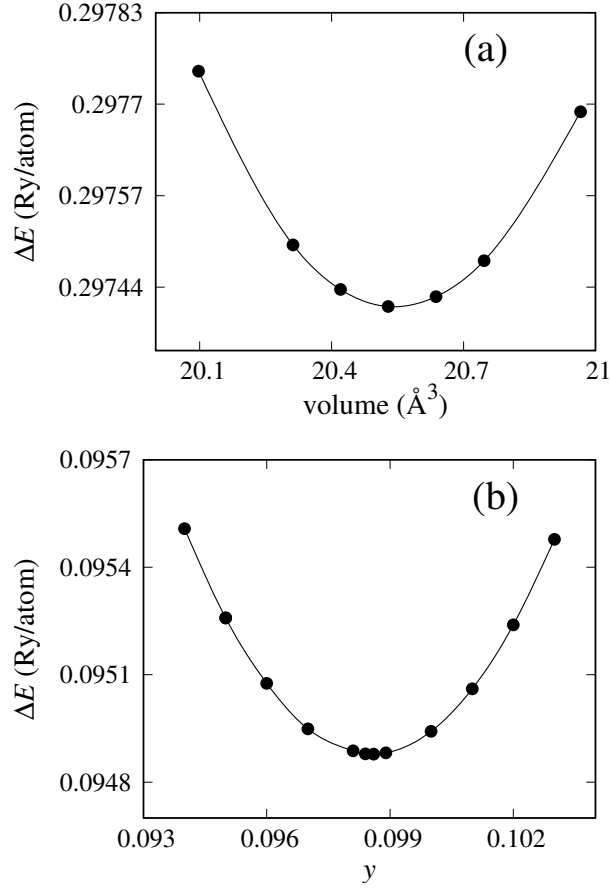


**Figure 3.4.** (a) Calculated total energy as a function of volume for  $\alpha$  uranium. (b) Calculated total energy as a function of the positional parameter  $y$  for  $\alpha$  uranium. The calculation of  $y$  is constrained to an equilibrium volume of 20.49  $\text{\AA}^3$ .

cell (DAC) experiments of Yoo *et al.* [46], which reported a bulk modulus of 135.5 GPa. Our pseudopotential-based results are in close agreement with the all-electron FP-LMTO calculations of Söderlind [8], which gave an equilibrium volume of 20.67  $\text{\AA}^3$  and a bulk modulus of 133.0 GPa. A published PAW-based pseudopotential from Beeler *et al.* [20] yields an equilibrium volume of 19.92  $\text{\AA}^3$ , which is lower than our result and farther from both the experimental value and the result from all-electron calculations.

The elastic moduli predicted by our pseudopotential are presented in Table 3.2. Like all materials with orthorhombic symmetry,  $\alpha$ -U has nine unique elastic moduli. Our model overestimates most of the elastic moduli relative to experiments. The three primary-direction



**Table 3.2.** Ground-state properties and elastic moduli of  $\alpha$ -U from present work, compared with the PAW pseudopotential calculations of Beeler *et al.* [20], the full-core calculations of Söderlind [8], and experiments from Barrett [15], Le Bihan *et al.* [43], and Fisher and McSkimin [47] (295 K).

	Theory			Experiment		
	present work	Beeler [20]	Söderlind [8]	Barrett [15]	Le Bihan [43]	Fisher [47]
$a$ (Å)	2.834	2.793	2.845	2.836	2.8553	-
$b$ (Å)	5.862	5.849	5.818	5.867	5.8702	-
$c$ (Å)	4.932	4.893	4.996	4.936	4.9568	-
$\gamma$	0.0986	0.097	0.103	0.102	0.102	-
volume/atom (Å <sup>3</sup> )	20.48	19.987	20.674	20.535	20.770	-
$B$ (GPa)	132.1	151	133	-	104(2)	-
$B'$	5.27	-	5.4	-	6.2	-
$C_{11}$ (GPa)	315	299	300	-	-	215
$C_{22}$ (GPa)	213	231	220	-	-	199
$C_{33}$ (GPa)	387	364	320	-	-	267
$C_{44}$ (GPa)	135	100	150	-	-	124
$C_{55}$ (GPa)	87	150	93	-	-	73
$C_{66}$ (GPa)	104	132	120	-	-	74
$C_{12}$ (GPa)	58	59	50	-	-	46
$C_{13}$ (GPa)	45	30	5	-	-	22
$C_{23}$ (GPa)	146	144	110	-	-	108

elastic moduli ( $C_{11}$ ,  $C_{22}$ , and  $C_{33}$ ) show good agreement with other theoretical results and with experiment, though all three principal elastic moduli are overestimated. The order ( $C_{33} > C_{11} > C_{22}$ ) of these three elastic moduli is also consistent with experiments. For  $C_{55}$  and  $C_{13}$ , the present results also show good agreement with experiments. The value of  $C_{66}$  is overestimated relative to experiment, but closer than any existing prediction from a pseudopotential-based calculation. The other elastic moduli are generally similar to existing theoretical predictions.

### 3.6.2 $\gamma$ -U: Crystal Structure and Elastic Moduli

The structure of  $\gamma$ -uranium at high temperature was first elucidated by Wilson and Rundle [48] at Iowa State University in 1949 using powdered uranium at 800 °C. The  $\gamma$  phase of uranium has a body-centered cubic (bcc; Strukturbericht designation A2) structure with

**Table 3.3.** The equilibrium lattice parameters and volume per atom of  $\gamma$ -uranium. Results are compared with the PAW pseudopotential calculations of Beeler *et al.* [20] and Taylor [11], as well as the norm-conserving pseudopotential calculations of Crocombette *et al.* [7] and the experiments of Wilson and Rundle [48] at room temperature. Elastic moduli are compared with previous PAW pseudopotential calculations from Beeler *et al.* [20] and Taylor [11].

	Theory				Experiment	
	present work	Beeler [20]	Taylor [11]	Crocombette [7]	Wilson [48]	Yoo [46]
$a$ (Å)	3.45	3.427	3.43	3.37	3.47	-
volume/atom (Å <sup>3</sup> )	20.56	20.124	20.18	19.14	20.89	-
$C_{11}$ (GPa)	40	86	161	-	-	-
$C_{12}$ (GPa)	145	155	184	-	-	-
$C_{44}$ (GPa)	42	37	56	-	-	-
$B$ (GPa)	110	132	176	170	-	113.3

two atoms in the standard unit cell [49, 50]. It is thermodynamically stable from 1050 K to the melting point of 1406 K [46].

In the nuclear fuels community,  $\gamma$  uranium is preferred to  $\alpha$ -uranium because it undergoes isotropic thermal expansion and radiation-induced swelling [51]. As Wilson and Rundle observed [48], it is not possible to quench pure  $\gamma$ -uranium to room temperature, but a metastable bcc phase can be retained at room temperature in U–Mo alloys. Recently, it was found that the bcc structure can be retained by alloying uranium with other metals, such as platinum, palladium, niobium, and zirconium [52]. In particular, the eutectoid point of  $\gamma$ -uranium with molybdenum impurities is at approximately 89 weight-percent uranium; to take advantage of the depressed phase transition temperature (and the associated increase in stability of the bcc phase), uranium alloyed with 10 wt% molybdenum ( $\approx 21.6$  at.%; U-10Mo) is currently being developed as a potential high-density low-enrichment uranium (LEU) fuel for high-performance research reactors. The lattice parameters, volume per atom, and elastic moduli as calculated with our pseudopotential-based model are presented in Table 3.3.

The lattice parameters for  $\gamma$ -uranium as calculated with the pseudopotential presented here are in good agreement with experiments. The elastic moduli are comparable with those of Beeler *et al.* [20] and Taylor [11]. The value of  $C_{12}$  is larger than that of  $C_{11}$ ,

**Table 3.4.** The optimized lattice parameters ( $\text{\AA}$ ), volume per atom ( $\text{\AA}^3$ ) and elastic moduli of bct uranium. Our calculated results are compared with those of Beeler *et al.* [20], Li *et al.* [19], Xiang *et al.* [16], and Söderlind [56].

	present work	Beeler [20]	Li [19]	Xiang [16]	Söderlind [56]
$a$ ( $\text{\AA}$ )	3.44	3.695	3.72	-	-
$c/a$	0.8125	0.8	1.24	-	0.82
volume/atom ( $\text{\AA}^3$ )	20.44	20.268	31.896	20.5	-
$C_{11}$ (GPa)	270	264	230	-	-
$C_{33}$ (GPa)	257	254	204	-	-
$C_{12}$ (GPa)	65	55	61	-	-
$C_{13}$ (GPa)	32	68	61	-	-
$C_{44}$ (GPa)	59	56	79	-	-
$C_{55}$ (GPa)	71	56	39	-	-
$B$ (GPa)	115.4	130	114	-	-

which is a violation of one of the stability criteria for cubic crystals ( $C_{11} - C_{12} > 0$ ), often called the Born stability criteria [53, 54, 55]. This violation is expected, as the bcc phase of uranium is unstable at low temperatures. The experimental value of bulk modulus by Yoo *et al.* [46] is in good agreement with our result.

### 3.6.3 Body-centered Tetragonal Uranium

The  $\beta$ -phase of uranium is stable at atmospheric pressure between 935 and 1045 K [1]. Tucker [57] determined that it has a tetragonal structure with 30 atoms per unit cell, but his space group assignment was later disputed. The assignment of a space group remained a controversy until 1988, when Lawson and coworkers [1] published neutron powder diffraction results. The experimental difficulties lie in the preparation of a single crystal of  $\beta$ -uranium and the need to operate at high temperature. Single crystals of a  $\beta$ -uranium alloy containing 1.4 atom% chromium were created by Tucker [58] and quenched to room temperature, but he did not establish whether this alloy had the same crystal structure as pure  $\beta$ -uranium [1]. An overview of the development of the crystal structure of  $\beta$ -uranium is given by Donohue and Einspahr [59, 60]. The present consensus is that  $\beta$ -uranium has a

**Table 3.5.** The equilibrium lattice parameter, volume per atom, and elastic moduli of fcc uranium. Results are compared with PAW pseudopotential calculations of Beeler *et al.* [20], Taylor [11], and Crocombette *et al.* [7].

	present work	Beeler [20]	Taylor [11]	Crocombette [7]
$a$ (Å)	4.300	4.433	4.48	4.30
volume/atom (Å <sup>3</sup> )	21.765	21.774	22.48	19.88
$C_{11}$ (GPa)	67	46	184	-
$C_{12}$ (GPa)	130	144	267	-
$C_{44}$ (GPa)	38	40	28	-
$B$ (GPa)	108.7	111	239	148

tetragonal crystal structure with with space group  $P4_2/mnm$  (no. 136) and 30 atoms in the unit cell.

We chose to simulate a body-centered tetragonal structure instead of  $\beta$  uranium because of the latter's complexity and computational expense. A similar simplification was used in studies similar to ours [20, 19]. The bct structure has only two atoms per unit cell, and is therefore less computationally expensive than  $\beta$  uranium. The equilibrium lattice parameters of bct uranium are presented in Table 3.4, alongside values from Beeler *et al.* [20] and Li *et al.* [19]. The volume per atom agrees well with Beeler *et al.* but is significantly different from that of Li *et al.* Xiang *et al.* [16] also studied the bct structure of uranium, though they did not provide the equilibrium lattice parameter or  $c/a$  ratio; their value of the equilibrium volume per atom was 20.5 Å<sup>3</sup>, similar but larger than our value. Our  $c/a$  ratio is in good agreement with both Beeler *et al.* [20] (0.8) and Söderlind [56] (0.82).

### 3.6.4 Face-Centered Cubic Uranium

Face-centered cubic uranium does not exist in nature, but it is a reasonable way to check the pseudopotential. Beeler *et al.* [20] and Taylor [11] studied this structure as well, so we compare our results with theirs. Table 3.5 shows the equilibrium parameters and elastic moduli as calculated with our model and with several other published pseudopotentials.

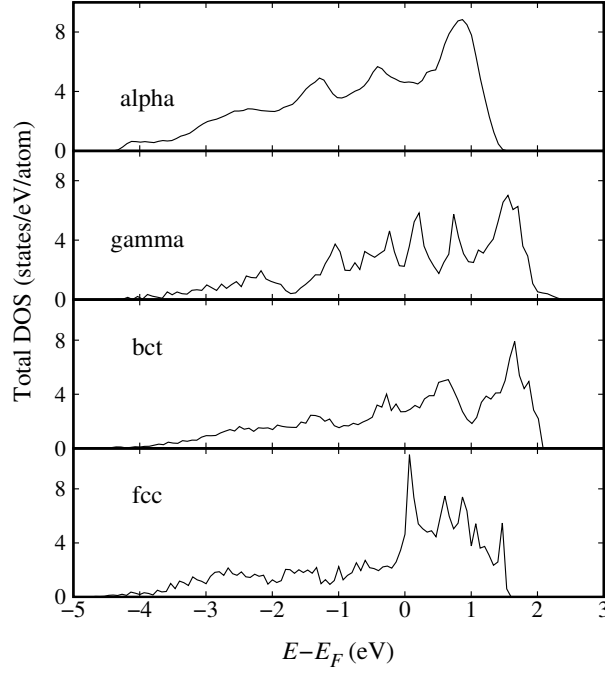


**Figure 3.5.** Total electronic densities of states of  $\alpha$ ,  $\gamma$ , bct, and fcc uranium near the Fermi level.

Our results are in good agreement with other pseudopotential calculations, particularly those of Beeler *et al.* [20]; the bulk modulus shows good agreement with their value as well. It should be noted that  $C_{12}$  is still higher than  $C_{11}$ , confirming that this model predicts the fcc phase to be unstable.

### 3.6.5 Electronic Density of States

The electronic densities of states (DOS) of  $\alpha$ , bct,  $\gamma$ , and fcc uranium are shown in Figure 3.5. The partial densities of states for the  $5f$  and  $6d$  orbitals are shown in Figure 3.6. We have only shown the partial densities of states for the  $5f$  and  $6d$  orbitals because these are the dominant orbitals near the Fermi level of uranium. There are also contributions from  $6s$ ,  $6p$ , and  $7s$  orbitals near the Fermi level, but these contributions are not as significant as the dominant  $5f$  and  $6d$  orbitals. Electrons near the Fermi level are important because

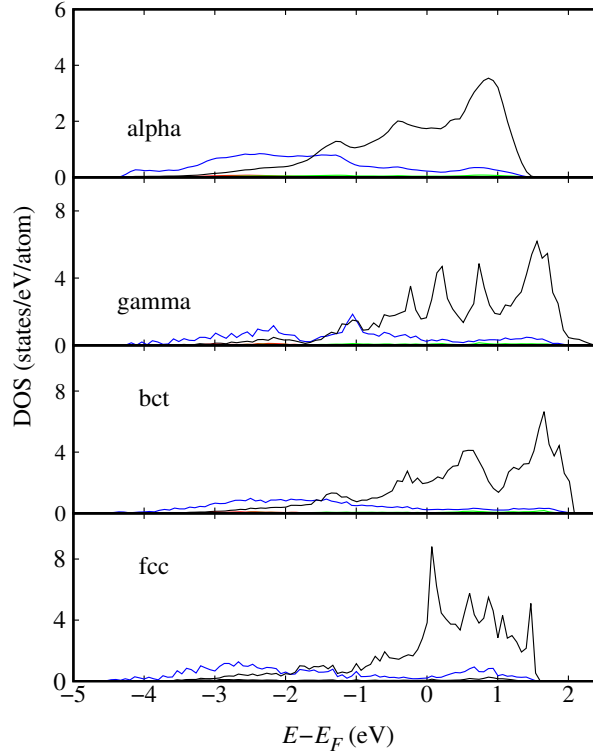


**Figure 3.6.** The partial electronic densities of states of  $\alpha$ ,  $\gamma$ , bct, and fcc uranium near the Fermi level. The  $6d$  (blue line) and  $5f$  (black line) electronic orbitals are shown. The  $s$  (red) and  $p$  (green) electronic orbitals are also included, but due to their very low contributions near the Fermi level, they are barely visible.

they are responsible for most of the metallic behavior. From Figure 3.5, it can be seen that the DOS spreads over energies between  $-4$  eV and  $2$  eV relative to the Fermi level. The density of states with our model is comparable to those calculated by Beeler *et al.* [20] and Xiang *et al.* [16]. For bcc and bct uranium, the  $f$  orbitals spread over a broader range of energies near the Fermi level and show multiple peaks above the Fermi level. The high density of states at energies above the Fermi level in the bct and  $\gamma$  phases suggest that these phases would be favored over  $\alpha$ -uranium at high temperature.

### 3.7 Conclusion

The equilibrium structures, cell volumes, and elastic moduli have been calculated using DFT with a newly parameterized pseudopotential model for four different uranium phases ( $\alpha$ ,  $\gamma$ , body-centered tetragonal, and face-centered cubic). Our results are either in good agreement with previous work or show improvement in comparison with experiments. Studying pure uranium is the first step in exploring different alloys of uranium that are of interest to the nuclear fuels community. Due to the lower cutoff energies that can typically be used, PAW-based pseudopotentials allow one to study larger supercells, which in turn provide more accurate studies of vacancy formation, grain boundaries, and fission gas transport.

According to our pseudopotential,  $\alpha$ -uranium is the lowest-energy crystal structure of the ones tested. The calculated elastic moduli show good agreement with previous DFT studies and experiments. Our model shows good agreement with previous pseudopotentials, but generally provides results that are either comparable to previously published pseudopotentials or closer to experimental values than previously published pseudopotentials. The three elastic moduli associated with shear ( $C_{44}$ ,  $C_{55}$ , and  $C_{66}$ ) show better agreement with experimental results than the tensile components. The lattice parameters of the bct structure are also very similar to those predicted by Beeler *et al.* [20], but they deviate significantly from those of Li *et al.* [19]. The elastic moduli show very similar trends to previously published models, apart from  $C_{23}$ , which is over-predicted by our model.

For  $\gamma$  uranium, which is of great interest for the development of low-enrichment uranium fuel, the lattice parameters are in close agreement with those of Taylor *et al.* [11] and with experiments. Apart from the elastic modulus  $C_{11}$ , the values of all computed parameters show very little discrepancy compared with those from the work of Taylor *et al.* [11] and Beeler *et al.* [20]. The bulk modulus shows very good agreement with experiment.

For fcc uranium, a hypothetical crystal structure, the computed lattice parameter is in close agreement with values reported by Beeler *et al.* [20] and by Crocombette *et al.* [7]. The equilibrium volume per atom does show a discrepancy from Crocombette but is in good agreement with Beeler *et al.* The elastic modulus  $C_{44}$  is also in good agreement with Beeler *et al.*, whereas  $C_{11}$  is intermediate between the value predicted by Beeler *et al.* and that predicted by Taylor *et al.* Lastly, the electronic density of states shows that the  $5f$  orbital partial density of states is the largest contribution to the total density of states at the Fermi energy, and the  $5f$  electrons therefore contribute the most to the bonding and conductivity of uranium. Most of the  $5f$  orbital electron density is spread over energies between  $-4$  and  $2$  eV relative to the Fermi level. We also find that  $\gamma$ -uranium has the highest density of states at values above the Fermi level, confirming that it should be favored at high temperature.

## References

1. A. C. Lawson, C. E. Olsen, J. W. Richardson, M. H. Mueller, and G. H. Lander. Structure of  $\beta$ -uranium. *Acta Crystallogr. B*, 44(2):89–96, 1988.
2. J. Akella, S. Weir, J. M. Wills, and P. Söderlind. Structural stability in uranium. *J. Phys. Condens. Matter*, 9(39):L549–L555, 1997.
3. G. H. Lander. G h lander. *Science*, 301:1057, 2003.
4. Arthur J. Freeman and G. H. Lander. *Handbook on the Physics and Chemistry of the Actinides*, volume 1,2. North-Holland, Amsterdam, 1984.
5. J. M. Wills and Olle Eriksson. Crystal-structure stabilities and electronic structure for the light actinides Th, Pa, and U. *Phys. Rev. B*, 45(24):13879, 1992.
6. Olle Eriksson, Per Söderlind, J. M. Wills, and A. M. Boring. First principles studies of crystal structures of  $f$  elements. *Phys. B Condens. Matter*, 190(1):5–11, 1993.
7. J. P. Crocombette, F. Jollet, L. Thien Nga, and T. Petit. Plane-wave pseudopotential study of point defects in uranium dioxide. *Phys. Rev. B*, 64(10):104107, 2001.
8. Per Söderlind. First-principles elastic and structural properties of uranium metal. *Phys. Rev. B*, 66(8):085113, 2002.



9. A. C. Lawson, B. M. Artinez, J. A. Roberts, B. I. Bennett, and J. W. Richardson, Jr. Melting of the light actinides. *Philos. Mag. B*, 80(1):53–59, 2000.
10. M. D. Jones, J. C. Boettger, R. C. Albers, and D. J. Singh. Theoretical atomic volumes of the light actinides. *Phys. Rev. B*, 61(7):4644, 2000.
11. Christopher D. Taylor. Evaluation of first-principles techniques for obtaining materials parameters of  $\alpha$ -uranium and the (001)  $\alpha$ -uranium surface. *Phys. Rev. B*, 77(9):094119, 2008.
12. P. E. Blöchl. Projector augmented-wave method. *Phys. Rev. B*, 50(24):17953–17979, December 1994.
13. J. P. Perdew, J. A. Chevary, S. H. Vosko, K. A. Jackson, M. R. Pederson, D. J. Singh, and C. Fiolhais. Atoms, molecules, solids, and surfaces: Applications of the generalized gradient approximation for exchange and correlation. *Phys. Rev. B*, 46(11):6671–6687, September 1992.
14. J. P. Perdew, J. A. Chevary, S. H. Vosko, K. A. Jackson, M. R. Pederson, D. J. Singh, and C. Fiolhais. Erratum: Atoms, molecules, solids, and surfaces: Applications of the generalized gradient approximation for exchange and correlation. *Phys. Rev. B*, 48(7):4978, 1993.
15. C. S. Barrett, M. H. Mueller, and R. L. Hitterman. Crystal structure variations in alpha uranium at low temperatures. *Phys. Rev.*, 129(2):625, 1963.
16. Shikai Xiang, Hanchen Huang, and L. M. Hsiung. Quantum mechanical calculations of uranium phases and niobium defects in  $\gamma$ -uranium. *J. Nucl. Mater.*, 375(1):113–119, 2008.
17. John P. Perdew, Kieron Burke, and Matthias Ernzerhof. Generalized gradient approximation made simple. *Phys. Rev. Lett.*, 77(18):3865–3868, October 1996.
18. John P. Perdew, Kieron Burke, and Matthias Ernzerhof. Generalized gradient approximation made simple (errata). *Phys. Rev. Lett.*, 78(7):1396, 1997.
19. J. H. Li, Q. B. Ren, C. H. Lu, L. Lu, Y. Dai, and B. X. Liu. Structure, formation energies and elastic constants of uranium metal investigated by first principles calculations. *J. Alloy Compd.*, 516:139–143, 2012.
20. Benjamin Beeler, Chaitanya Deo, Michael Baskes, and Maria Okuniewski. First principles calculations of the structure and elastic constants of  $\alpha$ ,  $\beta$  and  $\gamma$  uranium. *J. Nucl. Mater.*, 433(1-3):143–151, 2013.
21. Pierre Hohenberg and Walter Kohn. Inhomogeneous electron gas. *Phys. Rev.*, 136(3B):B864, 1964.
22. Llewellyn H. Thomas. The calculation of atomic fields. In *Mathematical Proceedings of the Cambridge Philosophical Society*, volume 23, pages 542–548. Cambridge University Press, 1927.

23. Enrico Fermi. Un metodo statistico per la determinazione di alcune prioriet  dell'atome. *Rend. Accad. Naz. Lincei*, 6(602-607):32, 1927.
24. David C. Langreth and John P. Perdew. The exchange-correlation energy of a metallic surface. *Solid State Commun.*, 17(11):1425–1429, 1975.
25. Walter Kohn and Lu Jeu Sham. Self-consistent equations including exchange and correlation effects. *Phys. Rev.*, 140(4A):A1133, 1965.
26. Paolo Giannozzi, Stefano Baroni, Nicola Bonini, Matteo Calandra, Roberto Car, Carlo Cavazzoni, Davide Ceresoli, Guido L. Chiarotti, Matteo Cococcioni, Ismaila Dabo, Andrea Dal Corso, Stefano de Gironcoli, Stefano Fabris, Guido Fratesi, Ralph Gebauer, Uwe Gerstmann, Christos Gougoussis, Anton Kokalj, Michele Lazzeri, Layla Martin-Samos, Nicola Marzari, Francesco Mauri, Riccardo Mazzarello, Stefano Paolini, Alfredo Pasquarello, Lorenzo Paulatto, Carlo Sbraccia, Sandro Scandolo, Gabriele Sclauzero, Ari P. Seitsonen, Alexander Smogunov, Paolo Umari, and Renata M. Wentzcovitch. QUANTUM ESPRESSO: A modular and open-source software project for quantum simulations of materials. *J. Phys. Condens. Matter*, 21(39):395502, September 2009.
27. Xavier Gonze, J-M Beuken, R. Caracas, F. Detraux, M. Fuchs, G-M Rignanese, Luc Sindic, Matthieu Verstraete, G. Zerah, F. Jollet, et al. First-principles computation of material properties: the abinit software project. *Comput. Mater. Sci.*, 25(3):478–492, 2002.
28. Conyers Herring. A new method for calculating wave functions in crystals. *Phys. Rev.*, 57(12):1169, 1940.
29. James C Phillips and Leonard Kleinman. New method for calculating wave functions in crystals and molecules. *Phys. Rev.*, 116(2):287, 1959.
30. D. R. Hamann, M. Schl ter, and C. Chiang. Norm-conserving pseudopotentials. *Phys. Rev. Lett.*, 43(20):1494, 1979.
31. Norman Troullier and Jos  Lu s Martins. Efficient pseudopotentials for plane-wave calculations. *Phys. Rev. B*, 43(3):1993, 1991.
32. Georg Kresse and D. Joubert. From ultrasoft pseudopotentials to the projector augmented-wave method. *Phys. Rev. B*, 59(3):1758, 1999.
33. N. A. W. Holzwarth, A. R. Tackett, and G. E. Matthews. A projector augmented wave (PAW) code for electronic structure calculations, part I: atompaw for generating atom-centered functions. *Comput. Phys. Commun.*, 135(3):329–347, 2001.
34. A. R. Tackett, N. A. W. Holzwarth, and G. E. Matthews. A projector augmented wave (PAW) code for electronic structure calculations, part II: pwpaw for periodic solids in a plane wave basis. *Comput. Phys. Commun.*, 135(3):348–376, 2001.

35. Nathalie Iché-Tarrat and Colin J. Marsden. Examining the performance of dft methods in uranium chemistry: Does core size matter for a pseudopotential? *The Journal of Physical Chemistry A*, 112(33):7632–7642, 2008.
36. Andrew M. Rappe, Karin M. Rabe, Efthimios Kaxiras, and J. D. Joannopoulos. Optimized pseudopotentials. *Phys. Rev. B*, 41(2):1227, 1990.
37. Naval Research Laboratories. Structure of Crystals. <http://aflowlib.duke.edu/users/egossett/lattice/>, 2015.
38. James D. Pack and Hendrik J. Monkhorst. “special points for Brillouin-zone integrations”—a reply. *Phys. Rev. B*, 16(4):1748–1749, 1977.
39. M. Methfessel and A. T. Paxton. High-precision sampling for Brillouin-zone integration in metals. *Phys. Rev. B*, 40(6):3616–3621, 1989.
40. P. Ravindran, Lars Fast, P. A. Korzhavyi, B. Johansson, J. Wills, and O. Eriksson. Density functional theory for calculation of elastic properties of orthorhombic crystals: Application to  $\text{TiSi}_2$ . *J. Appl. Phys.*, 84(9):4891–4904, 1998.
41. O. Beckstein, J. E. Klepeis, G. L. W. Hart, and O. Pankratov. First-principles elastic constants and electronic structure of  $\alpha\text{-Pt}_2\text{Si}$  and  $\text{PtSi}$ . *Phys. Rev. B*, 63(13):134112, 2001.
42. G. H. Lander, E. S. Fisher, and S. D. Bader. The solid-state properties of uranium: A historical perspective and review. *Adv. Phys.*, 43(1):1–111, 1994.
43. T. Le Bihan, S. Heathman, M. Idiri, G. H. Lander, J. M. Wills, A. C. Lawson, and Andreas Lindbaum. Structural behavior of  $\alpha$ -uranium with pressures to 100 GPa. *Phys. Rev. B*, 67(13):134102, 2003.
44. F. D. Murnaghan. The compressibility of media under extreme pressures. *Proc. Natl. Acad. Sci. U. S. A.*, 30(9):244–247, 1944.
45. Randolph Q. Hood, L. H. Yang, and John A. Moriarty. Quantum molecular dynamics simulations of uranium at high pressure and temperature. *Phys. Rev. B*, 78(2):024116, 2008.
46. Choong-Shik Yoo, Hyunhae Cynn, and Per Söderlind. Phase diagram of uranium at high pressures and temperatures. *Phys. Rev. B*, 57(17):10359, 1998.
47. E. S. Fisher and H. J. McSkimin. Adiabatic elastic moduli of single crystal alpha-uranium. *J. Appl. Phys.*, 29(10):1473–1484, 1958.
48. A. S. Wilson and R. E. Rundle. The structures of uranium metal. *Acta Crystallogr.*, 2(2):126–127, 1949.
49. Harry L. Yakel. Review of x-ray diffraction studies in uranium alloys. Technical report, Oak Ridge National Laboratory, Tennessee (USA), 1973.

50. I. Grenthe, J. Drozdzyński, T. Fujino, E. C. Buck, T. E. Albrecht-Schmitt, and S. F. Wolf. *The Chemistry of the Actinide and Transactinide Elements*, volume 1. Springer, Dordrecht, 2006.
51. J. H. Kittel, B. R. T. Frost, J. P. Mustelier, K. Q. Bagley, G. C. Crittenden, and J. Van Dievoet. History of fast reactor fuel development. *J. Nucl. Mater.*, 204:1–13, 1993.
52. N.-T. H Kim-Ngan and L. Havela. Superconductivity in U-T alloys (T = Mo, Pt, Pd, Nb, Zr) stabilized in the cubic  $\gamma$ -u structure by splat-cooling technique. *J. Sci. Adv. Mater. Dev.*, 1(2):121–127, 2016.
53. Max Born. On the stability of crystal lattices. I. *Proc. Camb. Phil. Soc.*, 36(2):160–172, 1940.
54. Max Born and Kun Huang. *Dynamical Theory of Crystal Lattices*. Clarendon Press, 1954.
55. Félix Mouhat and François-Xavier Coudert. Necessary and sufficient elastic stability conditions in various crystal systems. *Phys. Rev. B*, 90:224104, 2014.
56. Per Söderlind. Theory of the crystal structures of cerium and the light actinides. *Adv. Phys.*, 47(6):959–998, 1998.
57. C. W. Tucker, Jr. An approximate crystal structure for the beta phase of uranium. Technical Report KAPL-388, Knolls Atomic Power Laboratory, 1950.
58. C. W. Tucker. The crystal structure of the  $\beta$  phase of uranium. *Acta Crystallogr.*, 4(5):425–431, 1951.
59. Jerry Donohue and Howard Einspahr. The structure of  $\beta$ -uranium. *Acta Crystallogr. B*, 27(9):1740–1743, 1971.
60. Jerry Donohue. *Structures of the Elements*. John Wiley and Sons, 1974.

## **CHAPTER 4**

### **XENON MOBILITY IN BCC URANIUM IN THE PRESENCE OF MOLYBDENUM**

Understanding the fission gas diffusion in the fuel is one of the oldest challenges in nuclear engineering and fuel design. The presence of xenon gas (one of the fission gases) not only impact the neutronics of the reactor but also impact the thermal properties of the fuel. In U–Mo fuel fission gas shows an interesting pattern that stabilizes at high temperature (see section 2.1). The atomic transport process in U–Mo fuel is of great interest for understanding the performance of the fuel during irradiation. In particular, the fission gas behavior is an important factor since it reduces the thermal conductivity, and produce internal stress and blister. For  $\text{UO}_2$  fuel a large amount of work ([1, 2, 3]) have been performed to understand the mechanism of fission gas release. For metallic fuel (i.e U–Mo) the mechanism still needed to be studied.

In this study, we will focus on the atomic diffusion mechanism of xenon, which is the dominant gaseous species accounting for almost 85% of fission gas [4, 5]. We will approach this challenge with first principles technique. Point defects, especially vacancy defects, which is considered to be a major diffusion channel in the  $\text{UO}_2$  matrix [1]. Calculation of the vacancy formation energy in the  $\gamma$ -uranium would be a first step. And how the vacancy formation energy changes around the octahedral site is also important. The possible step would be calculating the energy needed to incorporate a xenon atom in one of the interstitial sites. Which particular location around the octahedral interstitial sites provide the stable location for xenon will be a really interesting to study. The formation energy of a single

vacancy in  $\gamma$ -U can be defined as

$$E_v = E_{(n-1)U} - \frac{n-1}{n} E_{nU} \quad (4.1)$$

Here  $E_{(n-1)U}$  is the total energy of an  $(n-1)U$  atom supercell containing a single uranium vacancy.  $E_{nU}$  is the total energy of an ideal  $\gamma$ -U supercell with  $n$  lattice sites. The formation energy of an U interstitial is defined as

$$E_I = E_{(n+1)U} - \frac{n+1}{n} E_{nU} \quad (4.2)$$

Where  $E_{(n+1)U}$  is the total energy of  $(n+1)U$  atoms, which includes the atoms at lattice positions as well as one interstitial. The formation energy of Mo substitution is defined as

$$E_s = E_{(n-1)U+Mo} - \frac{n-1}{n} E_{nU} - E_{Mo} \quad (4.3)$$

where  $E_{(n-1)U+Mo}$  is the energy of a lattice containing one Mo substitutional and  $E_{Mo}$  is the energy of one Mo atom in the bcc crystal. Incorporation of molybdenum in the  $\gamma$ -uranium would be a challenging step since U-Mo alloys are disordered. The energy needed to incorporate a free Xe atom at an octahedral interstitial site (OIS) in  $\gamma$ -U needs to be calculated. From this we might have an idea about a stable location of xenon. The calculation of vacancies and xenon can be investigated by the calculation of their migration energies.

The future work can be summarized but not limited to the following objectives.

- Vacancy formation energy for  $\gamma$ -uranium.
- The energy needed to incorporate a free xenon atom at an octahedral interstitial site (OIS) in  $\gamma$ -uranium.
- Stable location of xenon in the  $\gamma$ -uranium.

- Low energy position of xenon in the presence of molybdenum.
- Xenon migration energy calculation.
- Effect of xenon migration energy in the presence of molybdenum.
- Calculation of diffusion constant of xenon in  $\gamma$ -uranium.
- Impact of molybdenum in the diffusion constant of xenon.
- Xenon migration path analysis.

Using supercell approach in density functional theory is very time demanding. Some of the objectives presented above, usually are computationally heavy. Hopefully I can achieve the primary goals in 7-9 months.

## References

1. Thomas Petit, G. Jomard, C. Lemaignan, B. Bigot, and A. Pasturel. Location of krypton atoms in uranium dioxide. *J. Nucl. Mater.*, 275(1):119–123, 1999.
2. Jean-Paul Crocombette. Ab initio energetics of some fission products (kr, i, cs, sr and he) in uranium dioxide. *J. Nucl. Mater.*, 305(1):29–36, 2002.
3. M. Freyss, N. Vergnet, and T. Petit. Ab initio modeling of the behavior of helium and xenon in actinide dioxide nuclear fuels. *J. Nucl. Mater.*, 352(1-3):144–150, 2006.
4. A. T. Blades, W. H. Fleming, and H. G. Thode. The ratio of xenon to krypton in  $U^{235}$  fission. *Can. J. Chem.*, 34(3):233–237, 1956.
5. J. A. Petruska, H. G. Thode, and R. H. Tomlinson. The absolute fission yields of twenty-eight mass chains in the thermal neutron fission of  $U^{235}$ . *Can. J. Phys.*, 33(11):693–706, 1955.

# APPENDIX A

## CALCULATION OF ELASTIC PARAMETERS OF ALPHA-URANIUM

In this appendix, we will try to discuss the stress-strain relationships that was used to calculate the nine independent elastic constants of  $\alpha$ -uranium. The base-centered orthorhombic phase of uranium has three lattice parameters  $a$ ,  $b$ , and  $c$ , with the Bravais lattice vectors of the matrix form

$$\mathbf{R} = \begin{pmatrix} \frac{a}{2} & -\frac{b}{2} & 0 \\ \frac{a}{2} & \frac{b}{2} & 0 \\ 0 & 0 & c \end{pmatrix} \quad (\text{A.1})$$

Applying a small strain to the equilibrium lattice changes the total energy, and from this information the elastic parameters are deduced. The elastic parameters are identified as proportional to the second order coefficient in a polynomial fit of the total energy as a function of the distortion parameter  $\delta$  [1]. The distortion of lattice vector follows the rule  $\mathbf{R}' = \mathbf{R}\mathbf{D}$ . Here  $\mathbf{R}'$  is a matrix containing the components of the distorted lattice vectors and  $\mathbf{D}$  is the symmetric distortion matrix.

The internal energy of a crystal under strain,  $\delta$ , can be Taylor expanded in powers of the strain tensor with respect to initial energy of the unstrained crystal in the following way:

$$E(V, \delta) = E(V_0, 0) + V_0 \left( \sum_i \tau_i \xi_i d_i + 1/2 \sum_{ij} c_{ij} \delta_i \xi_i \delta_j \xi_j \right) + O(\delta^3) \quad (\text{A.2})$$



The unstrained volume is  $V_0$ , and  $E(V_0, 0)$  is the energy of the unstrained system. The Voigt notation has been used in the above equation, i.e.  $xx, yy, zz, yz, xz$  and  $xy$  are replaced with 1–6. Here  $yz, xz$  and  $xy$  are equation  $zy, zx$  and  $yx$  and for this reason  $\xi_i$  is equal to 1 for  $i = 1, 2$ , and 3 and 2 for  $i = 4, 5$  and 6.  $\tau_i$  is a component of stress tensor. The first three elastic constants  $c_{11}, c_{22}$  and  $c_{33}$  are obtained from the following distortions:

$$D1 = \begin{pmatrix} 1 + \delta & 0 & 0 \\ 0 & 1 & 0 \\ 0 & 0 & 1 \end{pmatrix} \quad (A.3)$$

$$D2 = \begin{pmatrix} 1 & 0 & 0 \\ 0 & 1 + \delta & 0 \\ 0 & 0 & 1 \end{pmatrix} \quad (A.4)$$

$$D3 = \begin{pmatrix} 1 & 0 & 0 \\ 0 & 1 & 0 \\ 0 & 0 & 1 + \delta \end{pmatrix} \quad (A.5)$$

The internal energies for these three distortions can be obtained from

$$E(V, \delta) = E(V_0, 0) + V_0 \tau_i \delta + \frac{V_0 C_{ii} \delta^2}{2} \quad (A.6)$$

The  $c_{44}, c_{55}$  and  $c_{66}$  are related to the distortion equations:

$$D4 = \begin{pmatrix} \frac{1}{(1-\delta^2)^{1/3}} & 0 & 0 \\ 0 & \frac{1}{(1-\delta^2)^{1/3}} & \frac{\delta}{(1-\delta^2)^{1/3}} \\ 0 & \frac{\delta}{(1-\delta^2)^{1/3}} & \frac{1}{(1-\delta^2)^{1/3}} \end{pmatrix} \quad (A.7)$$

$$D5 = \begin{pmatrix} \frac{1}{(1-\delta^2)^{1/3}} & 0 & \frac{\delta}{(1-\delta^2)^{1/3}} \\ 0 & \frac{1}{(1-\delta^2)^{1/3}} & 0 \\ \frac{\delta}{(1-\delta^2)^{1/3}} & 0 & \frac{1}{(1-\delta^2)^{1/3}} \end{pmatrix} \quad (\text{A.8})$$

$$D6 = \begin{pmatrix} \frac{1}{(1-\delta^2)^{1/3}} & \frac{\delta}{(1-\delta^2)^{1/3}} & 0 \\ \frac{\delta}{(1-\delta^2)^{1/3}} & \frac{1}{(1-\delta^2)^{1/3}} & 0 \\ 0 & 0 & \frac{1}{(1-\delta^2)^{1/3}} \end{pmatrix} \quad (\text{A.9})$$

These three elastic constants can be calculated from the corresponding internal energy:

$$E(V, \delta) = E(V_0, 0) + V_0 \tau_i \delta + \frac{V_0 C_{ii} \delta^2}{2} \quad (\text{A.10})$$

The last three distortions are:

$$D7 = \begin{pmatrix} \frac{1+\delta}{(1-\delta^2)^{1/3}} & 0 & 0 \\ 0 & \frac{1-\delta}{(1-\delta^2)^{1/3}} & 0 \\ 0 & 0 & \frac{1}{(1-\delta^2)^{1/3}} \end{pmatrix} \quad (\text{A.11})$$

$$D8 = \begin{pmatrix} \frac{1+\delta}{(1-\delta^2)^{1/3}} & 0 & 0 \\ 0 & \frac{1}{(1-\delta^2)^{1/3}} & 0 \\ 0 & 0 & \frac{1-\delta}{(1-\delta^2)^{1/3}} \end{pmatrix} \quad (\text{A.12})$$

$$D9 = \begin{pmatrix} \frac{1}{(1-\delta^2)^{1/3}} & 0 & 0 \\ 0 & \frac{1+\delta}{(1-\delta^2)^{1/3}} & 0 \\ 0 & 0 & \frac{1-\delta}{(1-\delta^2)^{1/3}} \end{pmatrix} \quad (\text{A.13})$$

The internal energies related with these three distortions are given by the following equations:

$$E(V, \delta) = E(V_0, 0) + V_0 [\tau_1 - \tau_2] \delta + \frac{1}{2} (c_{11} + c_{22} - 2c_{12}) \delta^2 \quad (\text{A.14})$$

$$E(V, \delta) = E(V_0, 0) + V_0 [\tau_1 - \tau_3] \delta + \frac{1}{2} (c_{11} + c_{33} - 2c_{13}) \delta^2 \quad (\text{A.15})$$

$$E(V, \delta) = E(V_0, 0) + V_0 [\tau_2 - \tau_3] \delta + \frac{1}{2} (c_{22} + c_{33} - 2c_{23}) \delta^2 \quad (\text{A.16})$$

The above equations can be used to calculate the remaining elastic constants  $c_{12}$ ,  $c_{13}$  and  $c_{23}$ .

## References

1. Duane C Wallace. *Thermodynamics of crystals*. Courier Corporation, 1998.